الجمهورية الجزائرية الديمقراطية الشعبية
République Algérienne Démocratique et Populaire
وزارة التعليم العالي و البحث العلمي
Ministère de l'Enseignement Supérieur et de la Recherche Scientifique
المدرسة الوطنية المتعددة التقنيات
École Nationale Polytechnique

Département d'Electronique

End-of-study project dissertation for obtaining the State Engineer's degree in Electronics

Developing Resilient Communication Architectures for the Internet of Underground Things (IoUgT)

Serine MEDJBER and Mohammed Amine LABBAS

Under the direction of Mr. Mourad ADNANE, Professor

Presented and defended publicly on 21/06/2025

Composition of the jury :

President	Mrs.	Rachida	TOUHAMI	Prof.	ENP
Promoter	Mrs.	Nour	KOUZAYHA	Dr	KAUST
Examiner	Mr.	Hicham	BOUSBIA-SALAH	A.Prof	ENP

ENP 2025

الجمهورية الجزائرية الديمقراطية الشعبية
République Algérienne Démocratique et Populaire
وزارة التعليم العالي و البحث العلمي
Ministère de l'Enseignement Supérieur et de la Recherche Scientifique
المدرسة الوطنية المتعددة التقنيات
École Nationale Polytechnique

Département d'Electronique

End-of-study project dissertation for obtaining the State Engineer's degree in Electronics

Developing Resilient Communication Architectures for the Internet of Underground Things (IoUgT)

Serine MEDJBER and Mohammed Amine LABBAS

Under the direction of Mr. Mourad ADNANE, Professor

Presented and defended publicly on 21/06/2025

Composition of the jury :

President	Mrs.	Rachida	TOUHAMI	Prof.	ENP
Promoter	Mrs.	Nour	KOUZAYHA	Dr	KAUST
Examiner	Mr.	Hicham	BOUSBIA-SALAH	A.Prof	ENP

ENP 2025

الجمهورية الجزائرية الديمقراطية الشعبية
République Algérienne Démocratique et Populaire
وزارة التعليم العالي و البحث العلمي
Ministère de l'Enseignement Supérieur et de la Recherche Scientifique
المدرسة الوطنية المتعددة التقنيات
École Nationale Polytechnique

Département d'Electronique

Mémoire de Projet de fin d'Etudes pour l'obtention du Diplôme d'Ingénieur d'Etat en Électronique

Développement d'Architectures de Communication Résilientes pour l'Internet des Objets Souterrains (IoUgT)

Serine MEDJBER and Mohammed Amine LABBAS

Sous la Direction de M. Mourad ADNANE, Professeur

Présenté et soutenu publiquement le 21/06/2025

Composition du jury :

Président	Mme.	Rachida	TOUHAMI	Prof.	ENP
Promoteur	Mme.	Nour	KOUZAYHA	Dr	KAUST
Examiner	Mr.	Hicham	BOUSBIA-SALAH	A.Prof	ENP

ENP 2025

ملخص

تُعد الاتصالات الموثوقة تحت الأرض تحديا نظرًا لتضاؤل الإشارة وظروف التربة المتغيرة. يقدم هذا العمل نظام مراقبة تحت أرضي يتميز باستهلاك جد قليل للطاقة وقابل للتوسع، يعتمد على الحثّ المغناطيسي ،(MI) ويُعزّز بجمع البيانات بواسطة طائرات بدون طيار .(UAV) يستخدم النظام المقترح مستقبلات تنبيه منخفضة الاستهلاك للطاقة، كما يُبقي جهاز الإرسال في وضع الإيقاف خلال فترات الخمول، مما يساهم بشكل كبير في إطالة عمر البطارية. تم بناء نموذج أولي باستخدام مكوّنات تجارية جاهزة، وأُجريت عدة تجارب لتقييم مدى الاتصال، ومعدل خطأ البت، واستهلاك الطاقة. أظهرت النتائج أن مدى التنبيه يمكن أن يصل إلى 6.8 متر، في حين يمكن تحقيق اتصال بيانات موثوق حتى مسافة 3.8 متر. علاوة على ذلك، يمكن لجهاز الإرسال أن يحقق عمرًا تشغيليًا يتجاوز 15 سنة. كما تم إجراء تحليل أداء واسع النطاق باستخدام الهندسة العشوائية لتقييم سلوك الشبكة. يوفر هذا النظام حلاً عمليًا للمراقبة طويلة المدى للبنى التحتية المدفونة.

كلمات مفتاحية : الحث المغناطيسي، إشارة الإيقاظ، الطائرات بدون طيار، كفاءة الطاقة، الهندسة العشوائية

Résumé

La communication fiable en milieu souterrain demeure un défi majeur en raison de l'atténuation élevée du signal et de la variabilité des conditions du sol. Ce travail propose un système de surveillance souterrain économe en énergie et évolutif basé sur l'induction magnétique renforcé par une collecte de données assistée par drone. Le système utilise des récepteurs à réveil ultra-basse consommation et maintient l'émetteur éteint lorsqu'aucune transmission n'est nécessaire, ce qui permet d'étendre considérablement la durée de vie des batteries. Un prototype a été réalisé à l'aide de composants commerciaux standards, et diverses expériences ont été menées afin d'évaluer la portée de communication, le taux d'erreur binaire et la consommation énergétique. Les résultats montrent que la portée du signal de réveil peut atteindre 6,8 mètres, tandis qu'une communication fiable est assurée jusqu'à 3,8 mètres, de plus, la durée de vie du transmetteur peut dépasser 15 ans. Une analyse à grande échelle basée sur la géométrie stochastique a également été réalisée pour étudier le comportement du réseau. Le système proposé constitue une solution pratique pour la surveillance à long terme des infrastructures enterrées avec une consommation énergétique minimale.

Mots clés : Induction magnétique, Drone, Efficacité énergétique, Géométrie stochastique.

Abstract

Reliable underground communication remains a major challenge due to high signal attenuation and variable soil conditions. This work presents a power-efficient and scalable underground monitoring system based on Magnetic Induction (MI), enhanced by Unmaned Aerial Vehicle (UAV)-assisted data collection. The proposed system uses ultra-low power wake-up receivers and keeps the transmitter off during idle periods to significantly extend battery lifetime. A prototype was built using commercial off-the-shelf components, and various experiments were conducted to evaluate communication range, bit error rate, and energy consumption. Results show that the wake-up range can reach 6.8 meters, while reliable data communication is achieved up to 3.8 meters, Furthermore, the transmitter can reach lifetimes exceeding 15 years. A large-scale performance analysis using stochastic geometry was also carried out to assess network behavior. This system provides a practical solution for long-term monitoring of buried infrastructure.

Keywords : Magnetic Induction (MI), Unmanned Aerial Vehicle (UAV), Power Efficiency, Stochastic Geometry.

Dedication

Three years of studying electronics were far from easy. In fact, they were often stressful and I don't think there is a single person who didn't feel imposter syndrome at least for a moment. But some people made this journey not only bearable, but better, easier, and even joyful.

First and foremost, thank you to my parents. Mama, thank you for always taking care of me, for bringing me food to my desk when I was so buried in work that I forgot to eat. Dad, thank you for all the rides to and from school-you spared me half my energy and so many worries.

To my sisters, Romaissa and Wiam, thank you for being inspiring role models since I was little, and for supporting and encouraging me every step of the way.

To my classmates, thank you for three unforgettable years filled with laughtereven in the toughest of times.

And last but not least, to Amine my partner, my binôme, for all these three years. Thank you for being the best teammate I could ever hope for. You taught me how to do things right, how to manage my stress, how to communicate, and every time we worked together, the outcome was always something to be proud of.

Thank you, all of you, from the bottom of my heart.

Serine

Dedication

To my beloved parents,

Since the day I was born, you have been my constant source of love, support, and guidance. You gave me everything; your time, your care, and the strength to pursue my dreams. You have always been by my side, creating the most favorable conditions for me to grow, learn, and succeed. This thesis is dedicated to you. It is my humble way of expressing gratitude and of hoping to give back a small part of what you have given me. I hope it brings pride to your eyes and joy to your hearts, as you have always brought to mine.

To my two brothers, Hamid and Hocine,
I am truly lucky to have you not only as brothers but also as best friends. You have always been a source of inspiration for me. For all the memories we shared, for all the childhood fights, for your help when I was young and clueless, and for your advice and support now. This thesis is for you.

To my best friends, the Y-22 Crew
To Yacine, Nassim, Hami, Lotfi, Reda and Nadir, I'm truly grateful to have you in my life. Someone once said, `"With Y-22, we can see the world with 16 eyes."` It's one of the most meaningful things ever said about our group. Since I joined the band in 2019, six years have passed and we're still the same. We've shared everything together: laughter, challenges, support, and unforgettable memories.
You are more than friends. You are my second family.
I dedicate this thesis to you.

To my classmates and all the ELN
Thank you for all the moments we've shared together. A special thanks to Ibrahim, Adel, Sidali, and Nadjib over the past three years, we've seen each other more than we've seen our own families. EUROBOT was one of the most incredible experiences of our journey, and I'm grateful to have lived it by your side. Thank you for everything.

To all merveleous person I met in ENP
I'm afraid to name names and accidentally forget someone others, so I'll simply say: thank you all. To everyone in the student club of my heart, ***CAP****, and to all those who supported me throughout these last five years, I am truly grateful.*

To my partner "El binôme"
Last but certainly not least, to my dear partner "El binôme" Serine, who has been exemplary, exceptional, and extremely supportive throughout our entire journey.
By her side, I learned that, no matter the circumstances, empathy, understanding, and communication are the true keys to success.
It wasn't easy to endure the pressure of our studies and the heavy workload, but by the

grace of God, everything we went through over the past three years helped us grow, learn, and achieve things we once thought impossible.

With all my love to you beautiful people,

Amine

Acknowledgements

This thesis marks the end of an important chapter in our lives and the beginning of a new one. We are deeply grateful to all those who contributed to the success of this work.

We would like to express our heartfelt thanks to our supervisors, Professor Mourad ADNANE and Professor Tareq Al-NAFFOURI, for making this internship possible. Your trust, guidance, and continuous support have been invaluable throughout this journey.

We also extend our sincere appreciation to Dr. Nour KOUZAYHA and Dr. Mahboob UR RAHMAN for their insightful advice and guidance during the internship period.

We are thankful to the head of our department, Mr Mohamed TAGHI, for his ongoing efforts in maintaining the quality and integrity of our academic environment.

Special thanks to Omar for his support and for generously sharing his experience, which greatly helped us during this project.

A heartfelt thank you to our school, *Ecole Nationale Polytechnique*. It has been an honor to be part of such a prestigious institution. We are proud to graduate from this school, and we carry its name with pride.

We also express our gratitude to all our teachers, from the preparatory classes to the final year, for their dedication and contributions to our academic and personal development.

Finally, we would like to thank God, for granting us the strength to overcome every challenge. Your guidance has accompanied us day by day, and we trust in You for the future that lies ahead.

Serine & Amine.

Contents

List of Tables

List of Figures

List of Abbreviations

AG2UG Aboveground-to-Underground. 20

BER Bit Error Rate. , 58, 61–64, 68, 69, 90

CPU Central Processing Unit. 32

DUT Device Under Test. 67

EM Electromagnetic. 17, 20–24, 27, 29, 31

IoT Internet of Things. 32

IoUgT Internet of Underground Things. 17, 18, 90

LED Light Emitting Diode. 28

LoS Line-of-sight. 28, 31

MCU Microcontroller Unit. 32, 34, 65

MI Magnetic Induction. , 17, 20, 24–27, 29, 31–34, 36, 38, 41, 42, 44, 75, 90

PPK2 Power Profiler Kit II. 54, 67

PPP Poisson Point Process. 75–77, 85

QoS Quality of Service. 58

RF Radio Frequency. 20, 24, 32–34

SPAD Single Photon Avalanche Diode. 28

UART Universal Asynchronous Receiver/Transmitter. , 44–46

UAV Unmanned Aerial Vehicle. 17, 32–34, 64, 90

UG2UG Underground-to-Underground. 20

USDA United States Department of Agriculture. 20

UWSN Underground Wireless Sensor Networks. 20, 21, 23, 24, 31

VLC Visible Light Communications. , 20, 21, 27–29

VWC Volume Water Content. , 22–24

WSN Wireless Sensor Networks. 20

WuC Wake up Call. 32–34, 46, 55, 60, 61, 70, 71, 79

General Introduction

Effective communication through soil remains a fundamental challenge due to severe signal attenuation, dynamic propagation characteristics, and multi-path effects. These limitations hinder the deployment of reliable underground monitoring systems, particularly for critical infrastructure such as pipelines.

The Internet of Underground Things (IoUgT) is redefining subsurface environment monitoring by enabling in-situ access to vital soil and infrastructure parameters. This paradigm opens the door to transformative applications in precision agriculture, environmental sensing, and buried infrastructure monitoring all domains where traditional surface-based measurements fall short.

This work proposes a power-efficient, scalable, and practical IoUgT monitoring solution leveraging Magnetic Induction (MI) technology. Unlike conventional electromagnetic (Electromagnetic (EM)) or acoustic methods, which are highly sensitive to soil composition and moisture levels, MI provides more robust performance in variable environments, resists environmental variability, and mitigates multi-path effects. However, one major limitation of MI is its short transmission range, which restricts its direct application in large-scale networks or dynamic terrains.

To address this, we introduce a hybrid IoUgT communication architecture that decouples underground sensing from long-range data collection. At the system's core are ultra-low-power, MI-enabled underground sensors equipped with wake-up receivers that remain in deep sleep until triggered, significantly reducing energy consumption. These underground nodes communicate with passive surface relay nodes that serve two essential functions: (1) initiating on-demand wake-up and data collection from buried devices, and (2) aggregating key measurements such as soil profiles and underground structural health indicators.

To further overcome the limitations of MI range and eliminate the need for fixed surface infrastructure, we integrate Unmanned Aerial Vehicle (UAV)s as mobile data collectors. UAVs fly over the surface relay nodes to retrieve aggregated data from the underground network and forward it to the cloud. This enables long-range communication, facilitates deployment in remote or inaccessible areas, and preserves energy at the surface level by maintaining short-range links.

In addition to the practical implementation, we also conducted a study of the systems large-scale behavior using stochastic geometry tools. This theoretical analysis allowed us to derive mathematical expressions for key evaluation metrics in large deployments, offering insights into scalability, performance limits, and design trade-offs.

This report is organized into six chapters:

- **Chapter 1: State of the Art** Reviews existing techniques for underground communication and highlights their limitations.
- **Chapter 2: System Concept and Architecture** Explains the reasons for choosing MI, introduces key terminologies, and describes the proposed hybrid system.
- **Chapter 3: Channel Modeling and Simulation** Presents the MI channel model, simulation results to explore the impact of physical parameters, and proposes a technique to enhance received power.
- **Chapter 4: Hardware Used** Details the commercial off-the-shelf components used to bring the system to life through prototyping and experimentation.

- **Chapter 5: Experimental Testbed and Implementation** Describes the experimental setups and testbeds used to evaluate the systems performance, including communication range and power efficiency.
- **Chapter 6: Large-Scale Network Analysis** Provides a theoretical evaluation of the system in large-scale deployment scenarios using stochastic geometry tools.

Together, these chapters build a comprehensive understanding of the proposed IoUgT system from physical implementation to theoretical scalability with a focus on enabling energy-efficient and reliable underground monitoring.

Chapter 1

State of the Art

1.1 Introduction

This chapter presents an overview of the main techniques used in underground wireless communication. It covers EM waves, acoustic waves, Magnetic Induction (MI), and Visible Light Communication (VLC). For each technique, we describe its operating principles, provide a basic channel model, and discuss its strengths and limitations.

1.2 Overview of Underground Wireless Communications

When the medium is soil, wireless nodes are buried beneath the surface and the variability of soil composition affect the signal propagation. The figure 1.1 shows 12 classes of soil textures, with a mixture of clay, silt, and sand with different proportions, as provided by (United States Department of Agriculture (USDA)) classification [1].

Figure 1.1: Different soil types by clay, silt, and sand composition as used by the USDA

Wireless underground communication can be categorized based on the type of link involved. In Underground-to-Underground (UG2UG) communication, all participating nodes are buried, and signal transmission must navigate the soil medium entirely. On the other hand, Aboveground-to-Underground (AG2UG) communication involves one node on the surface and one underground.This configuration introduces a transitional interface between air and soil.

Usually we use a network of sensors and when they work cooperatively to sense, compute, and communicate wirelessly with another node to share the data, we call it Wireless Sensor Networks (WSN)s. Underground Wireless Sensor Networks (UWSN)s extend this concept into the subsurface, enabling in-situ monitoring of soil conditions, buried infrastructure, and ecological processes.

Several wireless technologies are employed in underground communication, each with its strengths and limitations. Traditional Radio Frequency (RF) communication, MI,

Acoustic communication and VLC. Hybrid approaches that combine these modalities are under investigation to overcome individual limitations and to provide adaptive communication solutions. More details about these technologies are provided in the subchapters.

The flexibility of UWSNs allows them to be tailored for continuous monitoring, as in smart agriculture, or for event-driven applications, such as detecting structural failure or seismic activity. The range of applications for UWSNs is vast and continues to expand. *In agriculture*, they enable precision irrigation, fertilizer optimization, and real-time soil health monitoring, contributing to increased crop yields and resource efficiency. *In environmental monitoring*, UWSNs are used for landslide prediction, groundwater contamination detection, and carbon sequestration assessment. *In civil engineering*, they help monitor the integrity of underground infrastructure such as pipelines, tunnels, and retaining walls. *Security applications* include intrusion detection and underground surveillance in high-value areas.

1.3 Electromagnetic (EM) waves

1.3.1 Description of the Technique

In terrestrial wireless communication, where the transmission medium is air, (EM) waves are the most commonly used technique for transmitting information. This is primarily due to their relatively low path loss in air, which allows signals to propagate over long distances with minimal attenuation. Moreover, the radio frequency spectrum offers a wide bandwidth, enabling high data rate transmission.

However, this changes when it comes to underground communication. The well established wireless signal propagation techniques using EM waves do not work well in this environment due to three problems: **high path loss**, **dynamic channel condition** and **large antenna size** [2] [3]

- **High path loss:** The RF propagation through underground soil follows complex propagation characteristics because of different materials present in soil such as rocks, clay, and tree roots, which causes signal diffraction, scattering [4] and multipath effects, which leads to severe signal attenuation. Moreover, since water is a conductive material, it absorbs EM signals.
- **Dynamic channel condition:** The path loss is highly dependent on numerous soil properties such as water content, soil makeup (sand, silt, or clay) and density, and can change dramatically with time (e.g., increased soil water content after a rainfall) and location (soil properties change dramatically over short distances). [3] Thus, the channel becomes hard to predict and estimate.
- **Large antenna size:** Path loss can be reduced when working in low frequencies. However, this requires large antennas which are not practical since they will be deployed underground due to space constraints and the difficulty of installing and maintaining.

1.3.2 Channel model

In free space, the propagation characteristics of EM signals is modeled using the Friis path loss model. This model is extended in the context of underground communication.

So, the received power P_r is given by: [4]

$$P_r = P_t + G_t + G_r - L_0 - L_s \tag{1.1}$$

Where:

- P_t is the transmit power.
- G_t and G_r are the gains of the transmitter and receiver, respectively.
- L_0 and L_s are the path loss in free space and the loss caused by the soil medium, respectively.

The total path loss can be expressed as follows: [4]

$$L_0 + L_s = 6.4 + 20log(d) + 8.69\alpha d + 20log(\beta) \tag{1.2}$$

Where:

- d is the Euclidean distance.
- α is the attenuation constant.
- β is the phase shift constant.

The attenuation and phase shift constants are given by: [4]

$$\alpha = 2\pi f \left(\frac{\mu\epsilon_r}{2} \left(\sqrt{1 + (\frac{\epsilon_i}{\epsilon_r})^2} - 1 \right) \right) \tag{1.3}$$

$$\beta = 2\pi f \left(\frac{\mu\epsilon_r}{2} \left(\sqrt{1 + (\frac{\epsilon_i}{\epsilon_r})^2} + 1 \right) \right) \tag{1.4}$$

Where:

- f is the frequency.
- μ is the permeability of free space.
- ϵ_i and ϵ_r are the dielectric constants of the soil. They are calculated using the Peplinski principle: $\epsilon_s = \epsilon_r + i\epsilon_i$ [5].

1.3.3 Strengths and Limitations

As we have seen in the previous subsection, the path loss of the channel model depends on the dielectric constants of the soil (ϵ_i and ϵ_r). The dielectric constant (ϵ_s) is a measure of a material's ability to store electrical energy in an electric field. In soils, the dielectric constant is highly influenced by moisture content and soil texture. [6]

The table 1.1 shows how this constant changes by changing the Volume Water Content (VWC) and the type of soil:

These significant variations in the dielectric constantboth across different soil types (which may coexist in the same deployment area) and across varying moisture levels (e.g., due to rainfall) highlight the highly dynamic nature of the underground EM channel. As a result, the channel characteristics are difficult to model deterministically and may vary over time and space, posing major challenges for reliable communication and robust system design.

Table 1.1: Comparative summary of dielectric constants for different soil types under varying moisture conditions (5%, 10%, and 15% VWC).
Data source: [6]

Soil Type	**5% VWC**	**10% VWC**	**15% VWC**
Sandy Soil	4.5	6.2	7.8
Loamy Soil	6.5	10.4	14.5
Clayey Soil	9.0	15.2	20.8
Silty Soil	7.0	11.1	16.0

1.4 Acoustic waves

1.4.1 Description of the Technique

As shown in the precedent section, EM waves suffer from the soil medium properties; the high attenuation and multipath, hence, the signal cant reach a high depth. Instead of EM waves, the acoustic waves were implemented in underwater applications [7], [8], [9], [10] but considering the underground scenario, where the soil is the medium, the acoustic based techniques have their pros and cons.
Establishing reliable acoustic communication links in Underground Wireless Sensor Networks (UWSNs) requires understanding the characteristics of the soil acoustic channel, whose propagation models are significantly more complex than those of underwater environments, mainly due to the inhomogeneous nature of soil, which comprises both solid particles and fluids. [4]

1.4.2 Channel Model

The attenuation process can be separated into two types of damping: geometric and material damping.

- **Geometric damping** depends on the type and the location of the vibration source and increases polynomially with distances.
- **Material damping** is related to properties of soil medium and vibration amplitudes, and typically increases exponentially with distances.

As a result, as the acoustic wave propagates through soil media, the sound intensity at distance d, denoted as $P(d)$, decreases from the initial intensity P_0 as Equation 1.5 ([11])

$$P(d) \propto \underbrace{\frac{1}{d^{\gamma}}}_{\text{Geometric}} \underbrace{e^{-\alpha d}}_{\text{Material}}, \tag{1.5}$$

where:

1. α: is the attenuation coefficient (in decibels/meter),
2. γ: typically has a value between 1 and 3, depending on the beam pattern of electroacoustic transceivers.

The inhomogeneous composition of the soil leads to **multiple interbed reflections and refractions**, in [11], the channel model used is illustrated in equation 1.6;

$$H(f) \propto \sum_{i=1}^{M} k_i e^{-\alpha_i \pi f d_i} e^{j2\pi f d_i / c_i}, \tag{1.6}$$

The idea was to estimate the soil parameters with Matrix Pencil method since it is a damped exponentials decomposition method.

where:

- k_i s refer to constant complex gains.
- α_i: the frequency independent attenuation coefficient.
- d_i: transceiver distance.
- c_i: the speed of the traveling mode of the acoustic signal along each of the i-th paths

Since the channel model depends on the soil and this later consists of multiple inhomogeneous layers, we can Either:

- Study the soil properties where we'd like to deploy our system [12]
- Estimate the parameters [11].

1.4.3 Strengths and Limitations

The low speed of sound and the presence of multi-path effects make communication particularly challenging in an uncluttered underground environment. Developing reliable acoustic communication links for underground wireless sensor networks (UWSNs) requires identifying the soil acoustic channel characteristics, which involve more complex propagation models than those used in underwater environments. This complexity arises because soil is an inhomogeneous medium composed of both solid particles and fluids. Moreover, if the soil has a high Volume Water Content (VWC), the acoustic signal may not propagate effectively [12]. Additionally, acoustic communications typically offer low data rates (in bits per second), which results in longer transmission times and, consequently, higher power consumption.

1.5 Magnetic Induction Communication

1.5.1 Description of the Technique

Besides RF and acoustics, another promising technology is MI communication, which was initially introduced for wireless communication in the ocean [13]. It has since gained attention for its potential to operate in harsh and complex environments such as underground, underwater, and intrabody applications [14], [15].

MI communication utilizes quasi-static magnetic fields generated by transmitting coils to induce a voltage in receiving coils. Unlike EM waves, MI is largely unaffected by the high dielectric loss and multipath fading caused by the inhomogeneous composition of soil. This makes it more robust in UWSN where conventional EM solutions fail.

1.5.2 Channel Model

In MI communications, the transmission and reception are accomplished with the use of a coil of wire, as shown in the first row in Figure 1.2, where a_t and a_r are the radii of the transmission coil and receiving coil, respectively; r is the distance between the transmitter and the receiver. [3]

The MI transmitter and receiver can be modeled as the primary coil and the secondary coil of a transformer, respectively, as shown in the second row in Figure 1.2, where M is the mutual induction of the transmitter coil and receiver coil; U_s is the voltage of the transmitters battery; L_t and L_r are the self inductions; R_t and R_r are the resistances of the coil; Z_L is the load impedance of the receiver. We use its equivalent circuit to analyze the transformer, as shown in the third row in Figure 1.2, where: [3]

$$Zt = R_t + j\omega L_t \tag{1.7}$$

$$Z_{rt} = Z'_t = \frac{\omega^2 M^2}{R_r + j\omega L_r + Z_L} \tag{1.8}$$

$$Zr = R_r + j\omega L_r \tag{1.9}$$

$$Z_{tr} = Z'_r = \frac{\omega^2 M^2}{R_t + j\omega L_t} \tag{1.10}$$

$$U_M = -j\omega M \frac{U_s}{R_t + j\omega L_t} \tag{1.11}$$

- Z_t and Z_r are the self impedances of the transmitter coil and the receiver coil, respectively.
- Z_{rt} is the influence of the receiver on the transmitter while $Z_{tr}$is the influence of the transmitter on the receiver.
- U_M is the induced voltage on the receiver coil.

In the equivalent circuit, the transmitting power is equal to the power consumed in the primary loop. The receiving power is equal to the power consumed in the load impedance Z_L. Both received power and transmitting power are functions of the transmission range r: [3]

$$P_r(r) = Re\{\frac{Z_L \cdot U_M^2}{(Z'_r + Z_r + Z_L)^2}\} \tag{1.12}$$

$$P_t(r) = Re\{\frac{U_s^2}{Z_t + Z'_t}\} \tag{1.13}$$

According to the transmission line theory, the reflections take place unless the line is terminated by its matched impedance. In the equivalent circuit described in 1.2, to maximize the received power, the load impedance is designed to be equal to the complex conjugate of the output impedance of the secondary loop, i.e.: [3]

$$Z_L = \overline{Z_r + Z'_r} \tag{1.14}$$

The following task is to find the analytical expression for the resistance, self and mutual induction of the transmitter and receiver coils. The resistance is determined by the material, the size and the number of turns of the coil: [3]

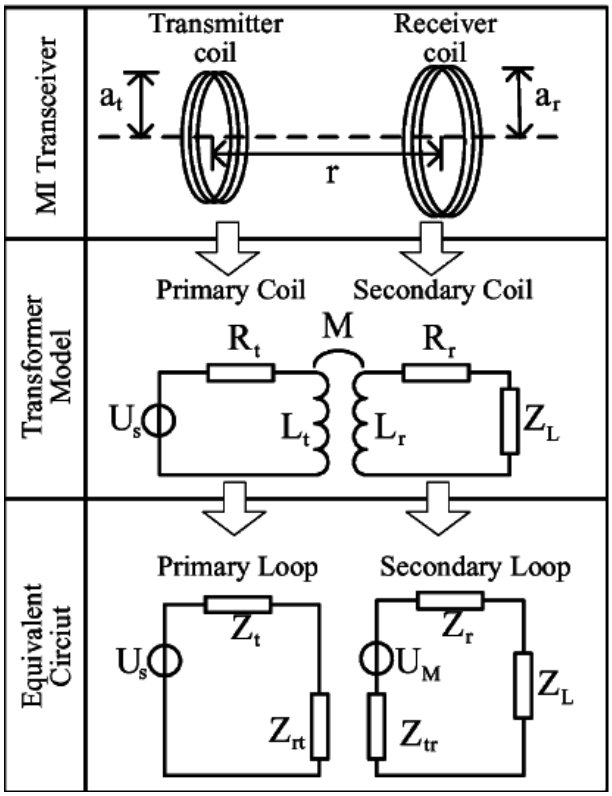

Figure 1.2: MI communication channel model

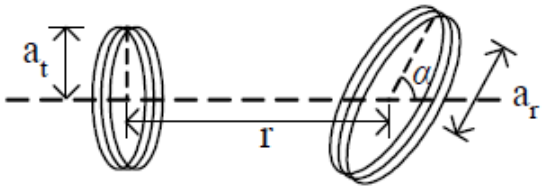

Figure 1.3: MI Transceiver

$$R_t = N_t \cdot 2\pi a_t \cdot R_0 \tag{1.15}$$

$$R_r = N_r \cdot 2\pi a_r \cdot R_0 \tag{1.16}$$

Where:

- N_t and N_r are the number of turns of the transmitter coil and receiving coil, respectively.
- R_0 is the resistance of a unit length of the loop.

Finally, the self induction expression is given by: [3]

$$L_t \simeq \frac{1}{2}\mu\pi N_t^2 a_t \tag{1.17}$$

$$L_r \simeq \frac{1}{2}\mu\pi N_r^2 a_r \tag{1.18}$$

And the mutual induction expression is given by [16]:

$$M \simeq \mu\pi N_t N_r \frac{a_t^2 a_r^2}{2r^3} \sin\alpha \simeq \frac{\sqrt{L_t \cdot L_r}}{r^3} \sin\alpha \tag{1.19}$$

Where $90° - \alpha$ is the angle between the axes of two coupled coils as shown in Figure 1.3.

1.5.3 Strengths and Limitations

It should be noted that, the underground transmission medium contains different type of soil, water, rocks and etc. According to [17], the substances of the underground medium can be categorized into four main groups including organic materials, inorganic materials, air, and water, where organic materials come from plants and animals; inorganic materials include sand, silt and clay. The relative permeabilities of the plants, animals, air and water are very close to 1. If the sand, silt, and clay do not consist of magnetite, their permeabilities are also close to 1. Since most soil in the nature does not contain magnetite, we can assume that the permeability of the underground transmission medium is a constant based on the above discussion which means the MI channel model can be considered constant unlike the EM and Acoustic channel models.

This can be further observed in Table 1.2 in which we can different types of soil with their typical value of permeability. All of these values are very close to 1 indeed.

Table 1.2: Typical values and ranges of relative magnetic permeability of various types of rock and soil.

Data source: [18]

Rock or soil type	**Typical value**	**Range**	**Source of information**
Soil and sedimentary rock (general)	1.0006	1.00001 to 1.001	Nettleton (1940)
Alluvium (NTS, Nevada)	1.004	1.0005 to 1.014	Monk (1965) (oral commun.)
Sandstone with unusually high magnetite content (Neroly Fm., California)	1.010	1.002 to 1.025	Bath (1965) (oral commun.)
Volcanic rock and soil (Amchitka Island, Alaska)	1.021	1.0001 to 1.053	Scott and Cunningham (1965) (written commun.)
Granite (Cheyenne Mtn., Colo.)	1.076	1.017 to 1.136	Scott (1965) (written commun.)
Rock in iron-mining areas (Sweden)	1.1	1.00001 to 14	Werner (1945)

1.6 VLC

1.6.1 Description of the Technique

VLC was standardized by IEEE in 2011 in the form of IEEE 802.15.7. The communication technology has been studied heavily in recent years, as it shows the potential to achieve a high transmission rate (i.e., 100 Mb/sec or even higher) for line-of-sight communications in clear media. [4]

Figure 1.4: VLC based IoUT for gas pipelines [5]

VLC is an emerging technology being investigated for underground communication, particularly in open underground spaces such as tunnels and gas reservoirs. In VLC systems, data is transmitted through modulated light, typically using LEDs, and received by photodetectors.

A system for down-hole monitoring consists of a (Light Emitting Diode (LED)s) were used at the bottom of the pipeline, and a single photon avalanche diode (Single Photon Avalanche Diode (SPAD)) was used as a receiver at the surface (see Fig. 1.4). [5]

1.6.2 Channel Model

One of the main requirements for effective VLC is a direct Line-of-sight (LoS) between the transmitter and the receiver. However, in underground environments, this is challenging due to physical obstructions and the heterogeneous nature of the medium. Moreover, the propagation of light is significantly affected by the presence of gas, dust, and moisture in underground settings, leading to scattering and absorption losses.

The received power in VLC-based systems [5], is typically modeled using Lambertian radiation patterns and is given by:

$$P_r = P_t \cdot \frac{(m+1)A}{2\pi d^2} \cdot \cos^m(\phi) \cdot T_s(\psi) \cdot g(\psi) \cdot \cos(\psi) \tag{1.20}$$

where:

- P_t is the transmitted optical power,
- m is the order of Lambertian emission,
- A is the detector area,
- d is the distance between LED and detector,
- ϕ is the angle of irradiance,
- ψ is the angle of incidence,
- $T_s(\psi)$ is the gain of the optical filter,
- $g(\psi)$ is the concentrator gain.

1.6.3 Strengths and Limitations

Despite its potential, VLC for underground communication is still in the experimental phase and faces practical limitations such as strict alignment requirements and sensitivity to environmental conditions. VLC requires line of sight, and its performance greatly deteriorates in the presence of obstacles. Because of this limitation, VLC cannot pass through the soil and is unusable for underground communication.

1.7 Conclusion

In this chapter, we reviewed the principal technologies explored for underground wireless communication, including EM waves, acoustic waves, MI, and VLC. For each technique, we discussed its fundamental principles, channel characteristics, and practical limitations in underground environments. Through this analysis, we highlighted the unique challenges posed by the underground medium, such as high signal attenuation, dynamic channel conditions, and deployment constraints.

Among the surveyed methods, magnetic induction communication emerges as a promising solution due to its resilience to soil variability, relatively stable channel behavior, and suitability for short- to medium-range communication. In the next chapter, we delve deeper into magnetic induction, detailing our rationale for selecting it as the focus of this work and exploring its potential for enabling reliable underground wireless networks.

Chapter 2

System Concept and Architecture

2.1 Introduction

In the previous chapter, we explored various techniques used for underground wireless communication, including electromagnetic waves, acoustic waves, visible light, and magnetic induction. Each of these approaches offers different trade-offs in terms of propagation characteristics, hardware requirements, and energy efficiency.

In this chapter, we justify our selection of magnetic induction as the communication technique best suited to our system's constraints and objectives. We begin by discussing the reasons behind this choice in light of the limitations associated with alternative methods. Then, we present an overview of our proposed system, which leverages a UAV-assisted relay architecture to enable energy-efficient data collection from buried sensor nodes. Additionally, we introduce key terminology and describe the core components involved in our design.

2.2 Choice of Communication Technique

As discussed in the previous chapter, various communication techniques can be employed for UWSN, including EM wave communication, acoustic communication, visible light communication, and MI. However, each of these methods presents significant limitations when used in underground environments.

EM wave-based communication suffers from a highly dynamic and unpredictable channel model due to the heterogeneous nature of soil composition and moisture content. It also requires relatively large antennas for low-frequency operation, which is impractical for compact buried nodes. Moreover, EM waves experience substantial attenuation in soil, resulting in extremely high path loss, as previously discussed in Section 1.3.

Acoustic wave communication, while capable of penetrating soil, is also highly dependent on soil mechanical properties such as density and moisture content. These parameters can vary over time and space, making the acoustic channel similarly unpredictable. Furthermore, acoustic communication offers very low data rates, making it inadequate for applications requiring timely and reliable data transmission, as detailed in Section 1.4.

Visible light communication is another alternative, but it is only feasible in highly constrained underground environments such as plastic or glass pipes, where a direct LoS is maintained. In most real-world scenarios, this requirement renders VLC impractical. More details are provided in Section 1.6.

Given these limitations, we opted for **magnetic induction (MI)** as the communication technique for our system. MI presents several compelling advantages: it is largely unaffected by the electrical and mechanical properties of the surrounding soil, resulting in a stable and predictable channel model; it relies on small coil-based antennas, which are suitable for miniaturized buried nodes; and it does not suffer from multipath fading, a common issue in EM wave-based systems. These features make MI a highly reliable and energy-efficient solution for underground communication across a variety of soil conditions, as discussed in Section 1.5.

2.3 Terminology and System Components

2.3.1 Wake-up Call

In the context of the Internet of Things (IoT), minimizing power consumption is crucial, especially for battery-powered or hard-to-reach nodes. In many applications, continuous sensing is not necessary; instead, data is only needed at specific times. This leads to the concept of **on-demand** sensing, where an IoT node remains mostly inactive and is triggered to operate only when needed. To enable this, all components of the IoT node can be turned off except for a small, ultra-low-power receiver called a wake-up receiver. This receiver continuously listens for a specific signal pattern known as the Wake-up Call (Wake up Call (WuC)). When it detects this signal, it activates the rest of the node to perform sensing and transmit the required data. This approach greatly extends the device's operational lifetime while maintaining responsiveness to real-time demands.

2.3.2 Deep Sleep

In the context of microcontrollers, deep sleep mode refers to a highly energy-efficient state in which the core components of the microcontroller, such as the Central Processing Unit (CPU), clocks, and most peripherals, are powered down to minimize power consumption. Only a minimal set of circuitry remains active, typically including modules that can detect external events like interrupts. This mode is essential in low-power applications where the device is expected to operate for long periods on limited energy sources. In the context of our project, the microcontroller remains in deep sleep mode by default, consuming minimal power, until a WuC is received.

2.3.3 Underground Sensing Node

The underground sensing node is buried beneath the surface and equipped with sensors, an Microcontroller Unit (MCU) and an MI-based wake-up receiver and transmitter. Its primary function is to sense physical parameters (e.g., soil moisture, temperature), process the data, and transmit it upward upon activation.

2.3.4 Above-Ground Relay Node

The above-ground relay node serves as an intermediary between the underground node and the UAV. It is responsible for receiving RF wake-up calls from the UAV and transmitting MI-based wake-up signals to the underground node. It also forwards sensed data from the underground node to the UAV, effectively bridging the two domains.

2.3.5 UAV-Assisted Relay

The UAV-assisted relay is a mobile, drone-mounted communication unit capable of wirelessly initiating WuC and collecting data. It is especially useful in remote or difficult-to-access environments, eliminating the need for manual data retrieval. The UAV is equipped with RF transmission and reception modules to interact with above-ground nodes.

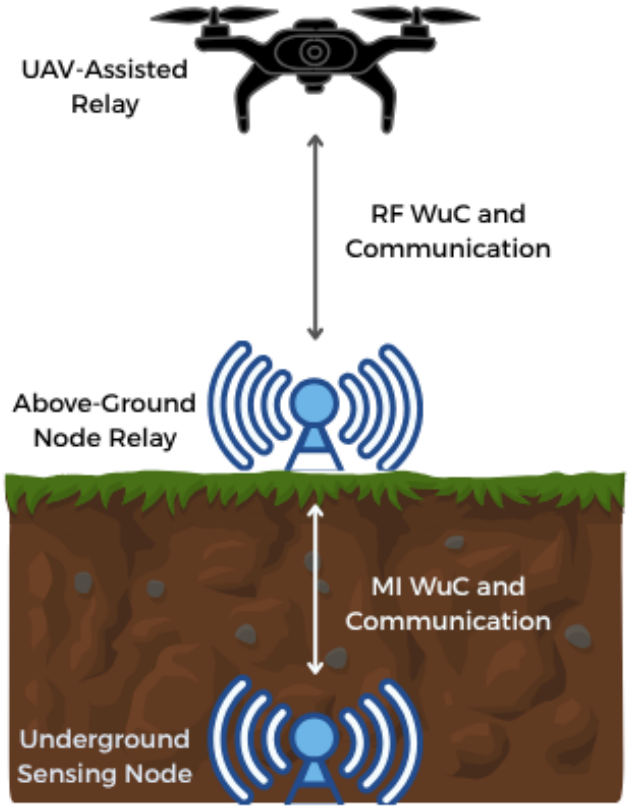

Figure 2.1: Our System

2.4 System Overview

This system enables energy-efficient data collection in hard-to-reach environments using a tiered communication structure. A UAV periodically visits the area and initiates communication by sending a WuC to an above-ground relay node. The relay node, once activated, forwards an MI-based wake-up signal to an underground sensing node. Upon activation, the underground node collects data, processes it, and transmits it back to the above-ground node, which then forwards it to the UAV. This approach avoids human intervention and extends the operational lifetime of buried sensors. An overview of the system architecture is illustrated in Figure 2.1.

2.5 Communication Flow

The communication sequence follows a top-down activation and bottom-up data transmission model:

1. The UAV flies near the deployment site and sends an RF WuC to the above-ground relay node.

2. The above-ground node receives the signal via its wake-up receiver and activates its MI transmitter.

3. The MI transmitter sends a WuC to the underground sensing node.

4. The underground node's wake-up receiver detects the signal, wakes up the MCU via interrupt, activates the sensors, processes the collected data, and triggers the MI transmitter.

5. The processed data is transmitted back to the above-ground node using MI communication.

6. Finally, the above-ground node forwards the data to the UAV using RF communication.

2.6 Conclusion

This chapter introduced the conceptual framework and architecture of our system. We began by comparing several underground communication techniques and explained why magnetic induction was selected as the most suitable option, thanks to its stability, low dependency on soil properties, and hardware efficiency. We then presented the key system components, including the UAV-assisted relay, the above-ground and underground nodes, and the role of wake-up calls and deep sleep in energy conservation. Finally, we detailed the overall system behavior and communication flow.

In the next chapter, we delve deeper into the physical layer by modeling the magnetic induction-based communication channel. This analysis will help us quantify performance and guide the design of the systems transmission and reception mechanisms.

Chapter 3

Channel Modeling and Simulation

3.1 Introduction

In the previous chapter, we introduced key terminologies relevant to our study, presented the overall system architecture, and explained the rationale behind choosing magnetic induction as our communication technique. We highlighted the advantages of MI in underground environments, particularly in terms of reliability and penetration through lossy media.

In this chapter, we delve deeper into the characteristics of the magnetic induction channel. We begin by presenting the MI channel model. We then simulate it to study the impact of various parameters on communication performance. Finally, we explore an enhancement technique known as 3D coils, which aims to improve signal reception under challenging deployment conditions.

3.2 Magnetic Induction Channel Model

We've seen in Section 1.5.2 that the MI communication channel can be modeled as a transformer circuit. In this section, we build upon that model by introducing a capacitor in series with the inductor, allowing the system to operate at a specific resonance frequency. Apart from this modification, the channel model remains as described previously.

The equivalent circuit, shown in the third row of Figure 1.2, is still used to analyze the system. The corresponding impedances are expressed as:

$$Z_t = R_t + j\omega L_t + \frac{1}{j\omega C_t} \tag{3.1}$$

$$Z_{rt} = Z'_t = \frac{\omega^2 M^2}{R_r + j\omega L_r + \frac{1}{j\omega C_r} + Z_L} \tag{3.2}$$

$$Z_r = R_r + j\omega L_r + \frac{1}{j\omega C_r} \tag{3.3}$$

$$Z_{tr} = Z'_r = \frac{\omega^2 M^2}{R_t + j\omega L_t + \frac{1}{j\omega C_t}} \tag{3.4}$$

$$U_M = -j\omega M \frac{U_s}{R_t + j\omega L_t + \frac{1}{j\omega C_t}} \tag{3.5}$$

To achieve resonance, the capacitor is selected such that:

$$j\omega L + \frac{1}{j\omega C} = 0 \tag{3.6}$$

Under this resonance condition, the imaginary parts cancel out, and the impedances simplify to:

$$Z_t = R_t \tag{3.7}$$

$$Z_{rt} = Z'_t = \frac{\omega^2 M^2}{R_r + Z_L} \tag{3.8}$$

$$Z_r = R_r \tag{3.9}$$

$$Z_{tr} = Z'_r = \frac{\omega^2 M^2}{R_t} \tag{3.10}$$

$$U_M = -j\omega M \frac{U_s}{R_t} \tag{3.11}$$

The load impedance becomes:

$$Z_L = \overline{Z_r + Z'_r} = R_r + \frac{\omega^2 M^2}{R_t} \tag{3.12}$$

The mutual inductive voltage squared is:

$$U_M^2 = \omega^2 M^2 \frac{U_s^2}{R_t^2} \tag{3.13}$$

From Equation 1.19, we have:

$$M^2 = \frac{L_t L_r}{r^6} \sin^2 \alpha \tag{3.14}$$

Substituting Equations 3.9, 3.10, 3.12, 3.14, and 3.13 into Equation 1.12, we obtain the received power as a function of distance:

$$\begin{aligned} P_r(r) &= Re\{\frac{Z_L \cdot U_M^2}{(Z'_r + Z_r + Z_L)^2}\} \\ &= \frac{(R_r + \frac{\omega^2 M^2}{R_t}) \cdot \omega^2 M^2 \frac{U_s^2}{R_t^2}}{4(R_r + \frac{\omega^2 M^2}{R_t})^2} \\ &= \frac{U_s^2}{4R_t} \cdot \frac{1}{1 + \frac{R_t R_r}{\omega^2 L_t L_r \sin^2 \alpha} r^6} \end{aligned}$$

Hence, the final expression for the received power is:

$$P_r(r) = \frac{P}{1 + Kr^6} \tag{3.15}$$

Where:

- $P = \dfrac{U_s^2}{4R_t}$.
- $K = \dfrac{R_t R_r}{\omega^2 L_t L_r \sin^2 \alpha}$.

We simulated the resonant magnetic induction channel model using MATLAB, employing the parameters shown in Table 3.1:

Table 3.1: Simulation Parameters for the MI Channel Model

Parameter	Value	Description
U_s	1 V	Source voltage
$R_t = R_r$	1 Ω	Coil resistances
L_t	0.5 mH	Inductance of transmitting coil
L_r	7.2 mH	Inductance of receiving coil
f	125 kHz	Operating frequency
ω	$2\pi \cdot 125 \cdot 10^3$ rad/s	Angular frequency
α	0°	Angle between the axes of the coils

Figure 3.1 shows the simulation results, where we plot the received power as a function of the distance between the transmitting and receiving coils.

As shown in Figure 3.1a, the received power decays rapidly with distance due to the r^{-6} dependency of the mutual inductance squared. The zoomed-in view in Figure 3.1b highlights this attenuation more clearly in the near-field region, which is of particular interest for buried or short-range communication systems.

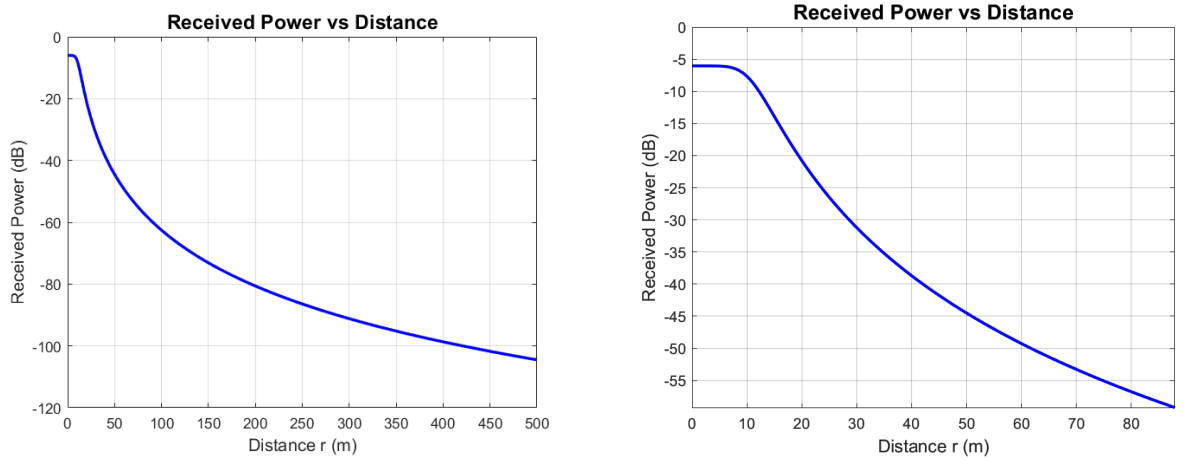

(a) Full-range view (0100 meters)

(b) Zoomed-in view (090 meters)

Figure 3.1: Received power vs. distance for the magnetic induction channel model: (a) full range and (b) zoomed-in view.

3.3 Effect of some parameters

After obtaining and simulating the magnetic induction channel model, we proceeded to study the impact of two key coil parameters: the number of turns N and the coil radius a. To simplify the analysis, we assumed that both the transmitter and receiver coils share identical values for N and a. We first fixed the radius to $a = 0.5$ m and varied the number of turns from 10 to 50 in order to evaluate how increased winding affects the received power. Then, we fixed the number of turns to $N = 50$ and varied the radius from 0.05 m to 0.5 m to observe the influence of coil size on performance.

3.3.1 Effect of the number of turns N

As illustrated in Figures 3.2a and 3.2b, the impact of increasing the number of coil turns N on the received power varies with distance. In the short range (04 meters), increasing N actually leads to reduced received power. However, beyond approximately 4 meters, increasing the number of turns becomes beneficial. The larger number of turns enhances the mutual inductance between the transmitter and receiver coils, improving the received power despite higher resistance. This trade-off highlights the importance of optimizing N based on the target communication range.

From the standard inductance formula shown in 1.18 and 1.17, we can see that as we increase the number of turns N, the coils self-inductance increases quadratically, strengthening the magnetic field generated:

$$L \propto N^2 \tag{3.16}$$

And from 1.16 and 1.15, the resistance also increases with N, but linearly. So while more turns slightly increase losses, it is not as significant as the gain in inductance:

$$R \propto N \tag{3.17}$$

From the channel model shown in Equation 3.15:

$$Pr(r) = \frac{U_s^2}{4R} \frac{1}{1 + \frac{R^2}{L^2\omega^2} r^6} \tag{3.18}$$

By analyzing the ratio in the denominator:

$$\frac{R^2}{L^2} \propto \frac{N^2}{N^4} = \frac{1}{N^2} \tag{3.19}$$

We conclude that as N increases, this ratio decreases, meaning the denominator becomes smaller. Thus, the received power becomes higher.

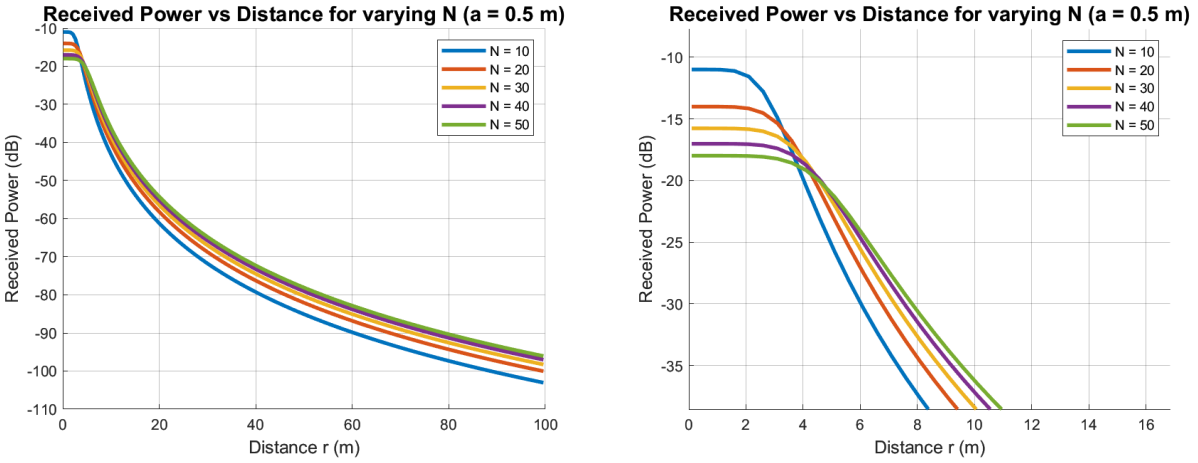

(a) Full-range view (0100 meters)

(b) Zoomed-in view (09 meters)

Figure 3.2: Received power vs. distance for the magnetic induction channel model varying the number of turns: (a) full range and (b) zoomed-in view.

3.3.2 Effect of the radius a

Next, we examined the impact of the coil radius a on the received power. As illustrated in Figures 3.3, increasing the coil radius leads to a noticeable decrease in the received power over distance. This behavior is attributed to the increased resistance associated with longer wire lengths at larger radii, which in turn reduces the power transfer efficiency of the magnetic induction link.

From Equations 1.18 and 1.17, we can see that the standard inductance increases linearly with the radius of th coil a:

$$L \propto a \tag{3.20}$$

And from Equations 1.16 1.15, we can see the resistances increases linearly with a as well:

$$R \propto a \tag{3.21}$$

By analyzing the ratio in the denominator of the channel model shown in Equation 3.18:

$$\frac{R^2}{L^2} \propto \frac{a^2}{a^2} = 1 \tag{3.22}$$

We can see that it is roughly a constant. However, the term $\frac{U_s^2}{4R}$ has an R in the denominator which is why the received power is decreasing.

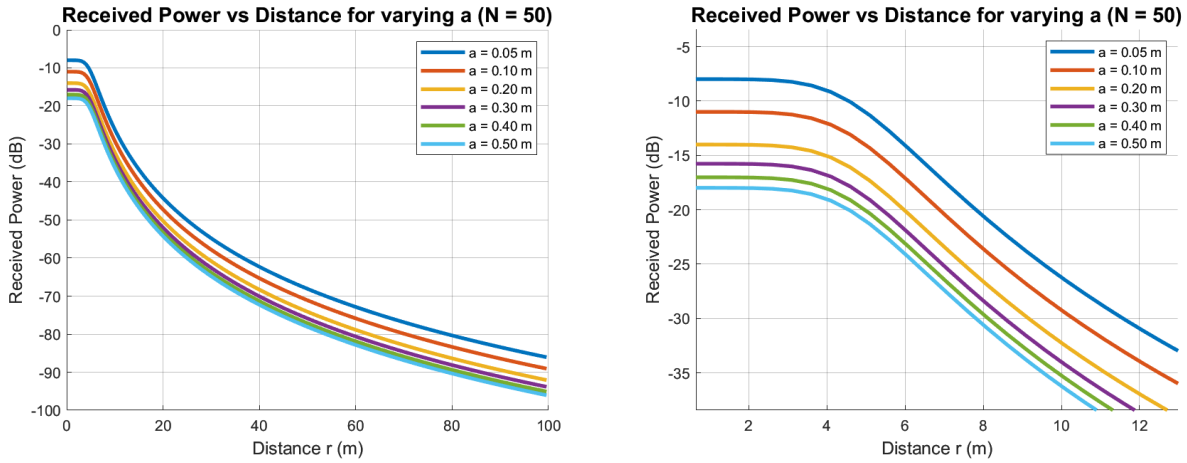

(a) Full-range view (0100 meters)

(b) Zoomed-in view (09 meters)

Figure 3.3: Received power vs. distance for the magnetic induction channel model varying the radii: (a) full range and (b) zoomed-in view.

3.3.3 Effect of the angle α

As we can see in Figure 3.4a, when the two coils are orthogonal ($\alpha = 0°$), the received power is essentially zero. This is expected, as the mutual inductance between the coils vanishes when their magnetic axes are perpendicular. However, Figure 3.4b also shows that as we gradually increase the value of α, the received power improves significantly. This trend continues until we reach the maximum value when the two coils are perfectly aligned ($\alpha = 90°$), where the coupling is strongest and the power transfer is most efficient.

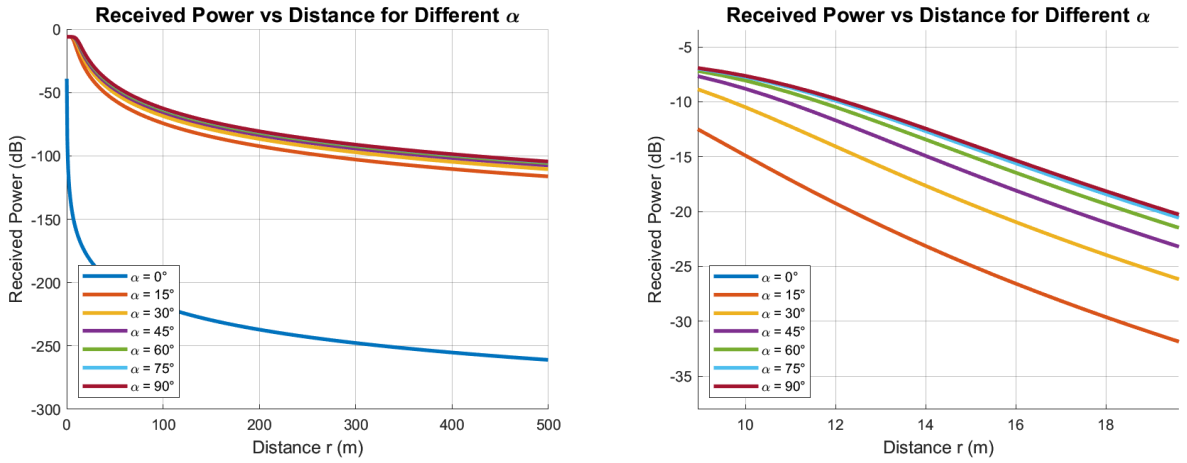

(a) Full-range view (0100 meters)

(b) Zoomed-in view (9-19 meters)

Figure 3.4: Received power vs. distance for the magnetic induction channel model varying the angle: (a) full range and (b) zoomed-in view.

3.4 3D Coils

A major challenge in underground MI communication systems is the sensitivity to coil misalignment. A "well-aligned" configuration means that the axes of the transmitter and receiver coils are parallel and directly face each other, which maximizes mutual inductance. The strength of the received signal strongly depends on the angle between the coil axes. However, in real underground deployments, maintaining such ideal alignment is often impractical due to irregular terrain, unpredictable orientations, or shifting over time. As a result, misalignment can significantly degrade communication performance.

Figure 3.5: Effect of coil misalignment on received signal strength

In Figure 3.5, two signals are shown: the pink waveform corresponds to a receiver coil that is well aligned with the transmitter, while the blue waveform comes from a misaligned receiver. We observe that the misaligned coil receives a significantly weaker signal. When the coils are misalignedmeaning their axes are no longer parallelthe mutual coupling efficiency decreases, leading to a reduction in received signal strength, as clearly seen in the blue waveform.

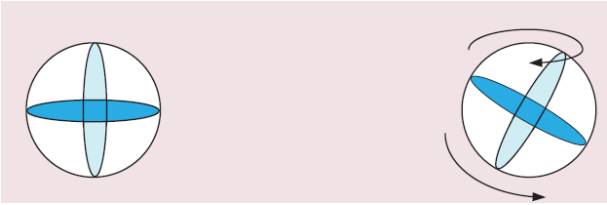

Figure 3.6: 3D MI communication
Data source: [16]

To address this issue, 3D MI coils have been proposed as a robust solution. As illustrated in Figure 3.6, these coils consist of three orthogonal windings. Each coil is aligned with one of the Cartesian axes (x, y, z), enabling the system to achieve omnidirectional coverage with just three coils, minimizing complexity and cost.

The coils include a series capacitor to ensure resonance. Because of their orthogonal orientation and field distribution, the coils do not interfere with one anothereach coils magnetic flux is nearly zero at the locations of the other two. At the receiver side, signals from the three independent coils are combined to improve signal strength.

Thanks to this configuration, the system maintains strong communication performance regardless of the relative orientation between the transmitter and receiver. At least one coil pair will always be well-aligned, ensuring reliable transmission even when the coils are rotated or deployed at arbitrary angles. This makes 3D coils particularly well-suited for complex and dynamic underground environments.

3.5 Conclusion

In this chapter, we explored the magnetic induction channel in detail. We began by presenting the theoretical model of MI-based communication and then simulated it to evaluate the influence of various system parameters. Through our analysis, we found that increasing the number of turns in the coils improves the signal strength and overall system performance. Conversely, increasing the coil radius leads to a decrease in performance, highlighting the need for careful coil design.

We also examined the critical impact of coil alignment on communication reliability. Misalignment between transmitter and receiver coils can significantly reduce the received signal strength. To address this challenge, we introduced the concept of 3D coils, which offer omnidirectional coverage and maintain strong communication regardless of orientation.

In the next chapter, we will shift our focus from the theoretical and simulated aspects to the practical implementation of the system. We will present the hardware components used to build the MI communication system and describe how they work together to enable reliable underground communication.

Chapter 4

Hardware Used

4.1 Introduction

In this chapter, we explore the hardware components of our system. For the communication module, we used two off-the-shelf resilient kits that operate using MI at 125 kHz: the *RF125 kit* from *NiceRF* and the *AS3933 demonstration kit* from *Sciosense*. As our microcontroller unit (MCU), we chose the *Firebeetle ESP32-C6*, which is widely used in IoT applications due to its efficient deep sleep mode. Finally, for sensing, we employed a *DHT-22* temperature and humidity sensor. However, depending on future application needs, any suitable sensor can be integrated into the system.

4.2 RF125 : Low Power Consumption Wireless Air Wake-Up

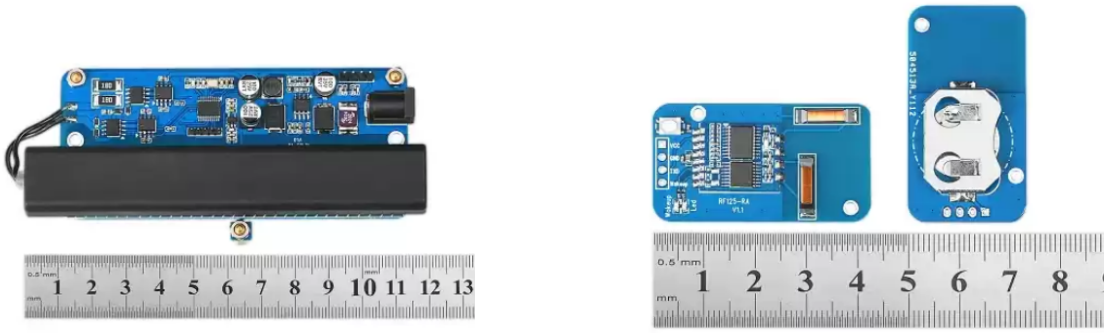

(a) The transmitter, RF125-TX

(b) The receiver, RF125-RA

Figure 4.1: RF125 kit

4.2.1 Transmitter's features (RF125-TX)

RF125 is a kind of wireless air wake-up 125KHz transmitter and receiver module launched by *NiceRF*, which is characterized by low-power and long-range(5-8 meters).

The kit that we used contains a RF125-TX (transmitter) and a RF125-RA (receiver), Figure 4.1).

The RF125-TX (see Sub-Figure 4.1a) is configurable through the UART communication protocol to:

- Change its ID.
- Change the interval between two transmissions.
- Send specific data.
- Start and stop transmission.

All the commands to configure the transmitter can be found in the Appendix A.

The transmitter encodes the data using Manchester coding. The baud rate was not specified, but based on oscilloscope analysis, it operates at 1024 symbols per second.

4.2.2 UART protocol for configuration

UART stands for universal asynchronous receiver/transmitter and defines a protocol, or set of rules, for exchanging serial data between two devices. UART is very simple and only uses two wires between transmitter and receiver to transmit and receive in both directions as shown in Figure 4.2a. Both ends also have a ground connection. Communication in UART can be simplex (data is sent in one direction only), half-duplex (each side speaks but only one at a time), or full-duplex (both sides can transmit simultaneously).

Data in UART is transmitted in the form of frames as shown in Figure 4.2b. Asynchronous means no shared clock, so for UART to work, the same bit or baud rate must be configured on both sides of the connection. Start and stop bits are used to indicate where user data begins and ends, or to frame the data. An optional parity bit can be used to detect single bit errors.

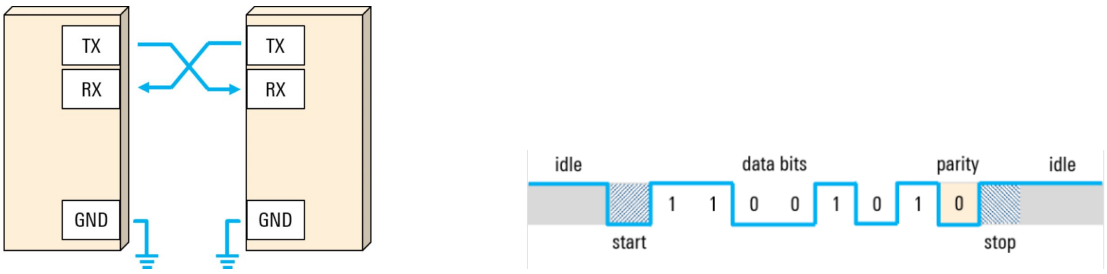

(a) UART wiring

(b) UART frame format

Figure 4.2: UART protocol
Data Source [19]

The UART parameters include: the baud rate, the number of data bits, the presence or absence of a parity bit, and the number of stop bits used to indicate the end of a data frame. In our case the RF125 has these parameters:

- **9600** - Baud rate (bits per second): The speed of data transmission is 9600 bits per second.
- **8** *Data bits*: Each transmitted data frame contains 8 data bits.
- **N** *Parity bit*: "N" stands for "No parity", meaning that no parity bit is used for error detection.
- **1** *Stop bit*: One stop bit is used to signal the end of each data frame.

4.2.3 Receiver's features (RF125-RA)

The RF125-RA is a low power consumption receiver equipped with two antenna (2D coil) to reduce the misalignment. It can work in two communiation modes: pairing mode or broadcast mode.
For the pinout, the RF125-RA has four pins, as shown in Figure 4.3. Through oscilloscope

RF125-RA

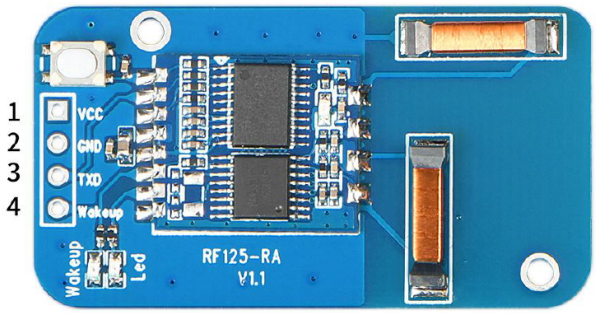

Pin number	Pin definition	I/O	Description
1	VCC		Can be externally connected with a positive voltage of 2.5-3.6V
2	GND		Power ground
3	TXD	O	Data output port
4	WAKE UP	O	After receiving 125K signal, output high pulse

Figure 4.3: RF125-RA Pinout

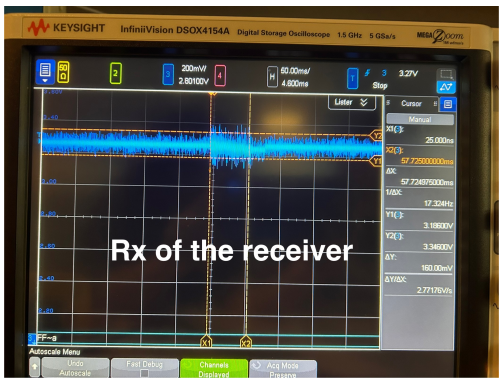

(a) The output of the *Rx* pin of the RF125-RA

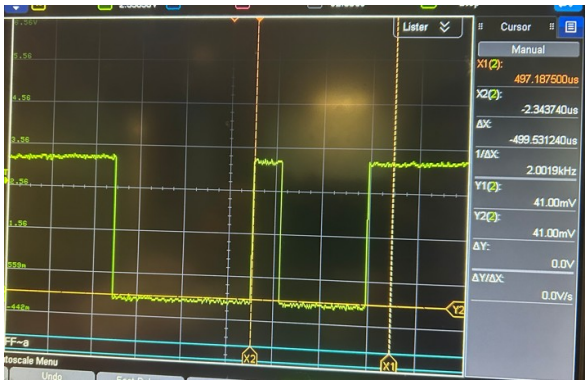

(b) The output of the *Tx* pin of the RF125-RA

Figure 4.4: Pins' output of the receiver RF125-RA

analysis, we obtained practical information about the output signals of these pins, which are shown in Figure 4.4.

As shown in subfigure 4.4a, the *Rx* pinwhich is expected to produce a high pulse when a WuC is receivedactually outputs a short pulse of a few millivolts, which can not be detected by a microcontroller.

Additionally, the *Tx* pin, which is expected to output the transmitted data, instead outputs only the length of the received data in 16-bit format. As shown in subfigure 4.4b, the pin remains high and, after receiving 8 bits of data, outputs 00001000. We confirmed this behavior by connecting the receiver's *Tx* pin to a microcontroller and printing the data using the Serial Monitor.

4.2.4 Communication Protocol

It is important to note that while the UART protocol is used to configure the two modules, the actual wireless communication between them follows a custom protocol. This communication is characterized by **On-Off Keying (OOK)** modulation, **Manchester**

encoding for data representation, and a well-defined **message packet structure**.

Modulation

The modulation scheme employed to the wake-up pattern is **On-Off Keying (OOK)**, a type of amplitude shift keying where:

- A **high signal** (carrier wave) represents a binary `1`,
- The **absence of a signal** (no carrier) represents a binary `0`.

Data Encoding

The data is encoded using **Manchester encoding**, which ensures synchronization and signal integrity. In this scheme:

- A binary `1` is represented by a **high-to-low** transition (`10`),
- A binary `0` is represented by a **low-to-high** transition (`01`).

This encoding removes DC bias and enables reliable asynchronous communication.

Message Packet Structure

The transmitted message consists of the following components:

1. **Carrier**: Continuous high level for 2.688 ms to 4.96 ms.

(a) The carrier according to the datasheet (b) The carrier observed with the oscilloscope

Figure 4.5: The carrier in the datasheet VS with the oscilloscope

2. **Separation Bit**: Low level for 0.5 ms.
3. **Preamble**: 5 repetitions of alternating 0.5 ms high and 0.5 ms low levels.

(a) The preamble according to the datasheet (b) The preamble observed in the oscilloscope

Figure 4.7: The preamble in the datasheet VS with the oscilloscope

(a) The separation bit after carrier according to the datasheet

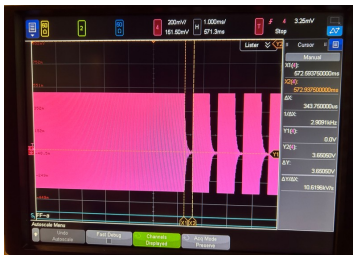

(b) The separation bit after carrier observed with the oscilloscope

Figure 4.6: The separation bit after carrier in the datasheet VS with the oscilloscope

(a) The pattern according to the datasheet

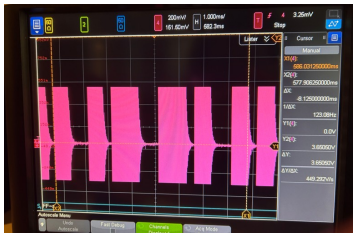

(b) The pattern observed in the oscilloscope

Figure 4.8: The pattern in the datasheet VS with the oscilloscope

4. **Pattern**: A 16-bit fixed synchronization code `0x9669` (binary: `1001011001101001`).

5. **Separation Bit**: Low level for 0.5 ms.

(a) Separation bit after the pattern according to the datasheet

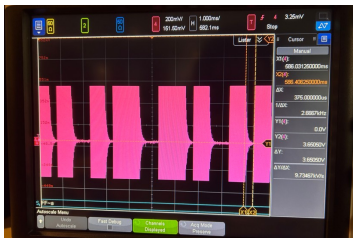

(b) Separation bit after the pattern observed with the oscilloscope

Figure 4.9: The separation bit after the pattern in the datasheet VS with the oscilloscope

6. **Data Packet** (Manchester encoded):
   - **H_id (1 byte)**: MSB indicates presence of data (`1` = data present), lower 7 bits represent the ID.
   - **Data Length (1 byte)**: Indicates the number of payload bytes (range: `0x00` to `0x2D`).
   - **Data (n bytes)**: Payload data.

- **Checksum (1 byte)**: Sum of all data bytes (modulo 256).

(a) The data packet according to the datasheet (b) The data packet observed with the oscilloscope

Figure 4.10: The data packet in the datasheet VS with the oscilloscope

7. **Separation Bit**: Low level for 0.5 ms.

Example:

- `H_id = 0x82` → MSB = 1 (data present), ID = `0x02`
- `Data Length = 0x05`
- `Data = 0x01, 0x02, 0x03, 0x04, 0x05`
- `Checksum = 0x0F` (sum of data bytes)

4.2.5 Power Consumption

To evaluate the power consumption of both the transmitter (RF125-TX) and the receiver (RF125-RX), we used the **Power Profiler Kit**, which is described in Appendix B which is a circuit used in IoT for measuring the consumption from μA up to 1A. The objective was to measure the current drawn by the devices during operation. The results are shown in Figure 4.11.

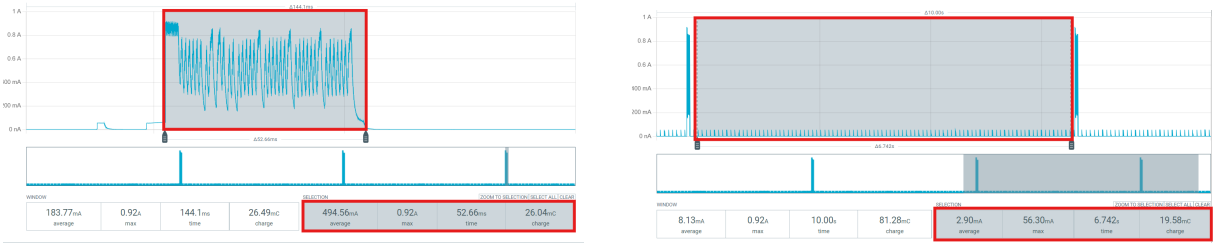

(a) Power consumption during transmission (b) Power consumption in standby mode

Figure 4.11: Power consumption of the transmitter

By fixing the interval time to 6 ms, we observed the following:

- **In the standby mode of the transmitter**: the average current consumption is 2.9 mA, with a maximum value of 56.30 mA as shown in the subfigure 4.11b.
- **In the transmission mode of the transmitter**: the current consumption is 494.56 mA for a duration of 52.66 ms, with a peak of 920 mA reached at the beginning of the transmission as illustrated in the subfigure 4.11a.

A comparison between the transmitter's power consumption based on datasheet specifications and practical measurements is shown in Table 4.1.

Table 4.1: *Theoretical vs. Practical* comparison of the power consumption of the RF125-TX

State	Theoretical	Practical
No transmission	$< 300\ \mu A$	2.9 mA
Transmission	< 300 mA	494.56 mA

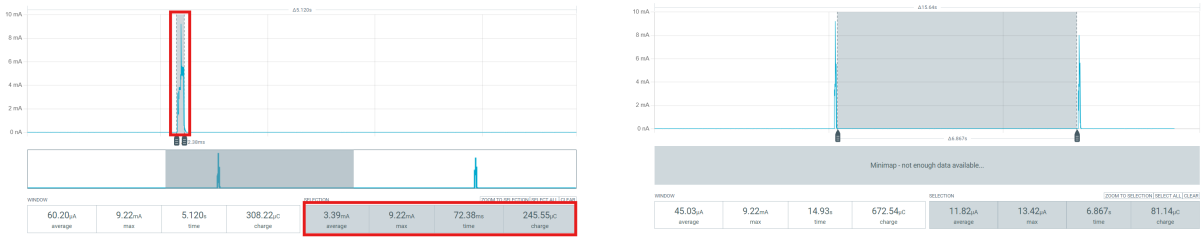

(a) Power consumption during reception

(b) Power consumption in standby mode

Figure 4.12: Power consumption of the receiver

- **In the standby mode of the receiver**: the average current consumption is 11.82 μA, with a maximum value of 13.42 μA as shown in the subfigure 4.12b.
- **During reception**: the current consumption is 3.39 mA for a duration of 72.38 ms, with a peak of 9.22 mA reached at the beginning of the transmission as illustrated in the subfigure 4.12a.

A comparison between the transmitter's power consumption based on datasheet specifications and practical measurements is shown in Table 4.2.

Table 4.2: *Theoretical vs. Practical* comparison of the power consumption of the RF125-RA

State	Theoretical	Practical
No reception	$< 9\ \mu$A	11.82 μA
Reception	< 3 mA	3.39 mA

4.2.6 Limitations

After exploring the RF125 kit, several limitations were identified:

- **Limited range:** The specified range is between 5 and 8 meters. However, tests showed that the actual range barely reaches 5 meters under typical conditions.
- **Receiver output:** The receiver only provides the length of the received data packet, without giving access to the actual data content.
- **Wake-up pulse limitations:** The wake-up pulse generated by the receiver is extremely brief and has a low voltage level, making it unsuitable for waking up a microcontroller from deep sleep mode.

- **Lack of documentation**: The available materials are either outdated, incomplete, or overly simplified, offering limited insight into the internal design, operating principles, and interfacing options of the system. Critical technical specificationssuch as coil characteristics and signal behavior under different load or distance conditionsare either poorly described or missing altogether

4.3 AS3933 Demoboard

The AS3933 Demoboard, shown in figure 4.13, is a complete evaluation platform for demonstrating the capabilities of the AS3933 low-frequency wake-up receiver IC. Operating at 125 kHz, it is designed to evaluate wake-up communication systems in low-power wireless applications. The kit includes both the receiver board (AS3933 Demoboard) and the 125 kHz Wake-up Transmitter Board, providing a full system for evaluation. The link for the user guide is provided in the appendix C and for more informations

Figure 4.13: AS3933 demoboard

4.3.1 Transmitter's features

Figure 4.14: 125 kHz Wake-up Transmitter Board

The 125 kHz Wake-up Transmitter Board, shown in Figure 4.14, is used to send wake-up patterns that the AS3933 can detect. It provides the following features:

- **Adjustable symbol rate:** From 512 to 4096 symbols/s.
- **Wake-up pattern generation:** Supports Manchester-coded patterns of 16 or 32 bits.

- **Transmission modes:**
  - *Single Pattern:* Sends a single wake-up sequence on demand.
  - *Pattern + Data:* Transmits a pattern followed by the data stream `01010101`.
  - *Automatic Mode:* Sends a wake-up pattern every 1 second.
- **User interface:** Includes buttons for manually triggering each mode.
- **Buzzer:** Emits a sound during transmission, aiding in range testing.
- **USB Interface:** Enables configuration via the graphical user interface (GUI).

4.3.2 Receiver's features

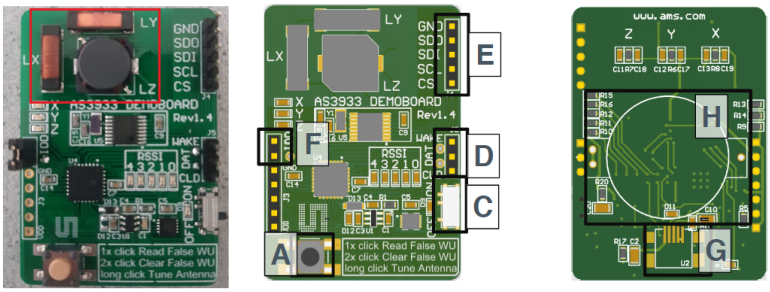

Figure 4.15: The receiver: AS3933 Demoboard

The AS3933 Demoboard, illustrated in the Figure 4.14, offers rich features for evaluating low-frequency wake-up applications:

- **Three-channel antenna input:** Supports X, Y, and Z axis coils for omnidirectional detection.
- **Manchester pattern matching:** Detects 16- or 32-bit patterns.
- **Data recovery:** Provides both data (DAT) and recovered clock (CL_DAT) outputs.
- **RSSI indicators:** Visual indication of signal strength and active channel through LEDs.
- **Antenna tuning:** Includes automatic resonance tuning to 125 kHz using internal capacitor banks (032 pF).
- **Low power modes:** Disable unused channels to reduce current consumption.
- **Configurable envelope detector and data slicer:** Tailors performance to bit rate and noise conditions.

4.3.3 Communication protocol

The AS3933 communicates via a low-frequency magnetic field modulated at 125 kHz using Manchester-coded data. The communication protocol includes:

- **Wake-up sequence:** A preamble followed by a Manchester-encoded pattern.
- **Pattern correlation:** Performed by the AS3933 correlator; an interrupt is triggered on a match.
- **SPI Interface:** Configuration and data access via SPI signals (CS, SCL, SDI, SDO).
- **Wake-up signal:** The WAKE pin is set high when a valid pattern is received.
- **Data interface:** Recovered data appears on the DAT pin and the corresponding clock on the CL_DAT pin.

Note: Symbol rate, pattern length, and correlator settings must be synchronized between transmitter and receiver for proper operation.

4.3.4 Power Consumption

The AS3933 is optimized for ultra-low-power wake-up applications:

- **Low current consumption:** Operates in the microampere range when in listening mode.
- **Battery operation:** Powered by a 3 V CR2032 coin cell.
- **Power measurement jumper:** The IDD jumper allows direct measurement of the receiver's current draw.
- **Power-saving modes:** Selective channel disabling and low-power configurations available via GUI.

4.3.5 Limitations

While the AS3933 Demoboard is highly functional, it comes with certain limitations:

- **Noise sensitivity:** Susceptible to interference from nearby sources (e.g., switching power supplies, lighting).
- **Complex configuration:** Many parameters (e.g., gain, slicer threshold, envelope time constant) must be manually optimized.
- **Environmental dependence:** Changes in temperature or electromagnetic environment can affect resonance and signal quality.

These limitations should be considered when designing robust LF wake-up systems, especially for applications with constraints such as underground or mobile environments.

4.4 ESP32 FireBeetle C6 Configuration and Flash Logging

The FireBeetle 2 ESP32-C6, shown in Figure 4.16, is a low-power IoT main control board based on the ESP32-C6 chip. Designed primarily for smart home and IoT applications, it supports multiple communication protocols, including Wi-Fi 6, Bluetooth 5, Zigbee 3.0, and Thread 1.3, enabling seamless integration with a wide range of networks and devices. The board also offers versatile power input options, including Type-C USB, 5V DC, and solar power, making it adaptable for various deployment environments.

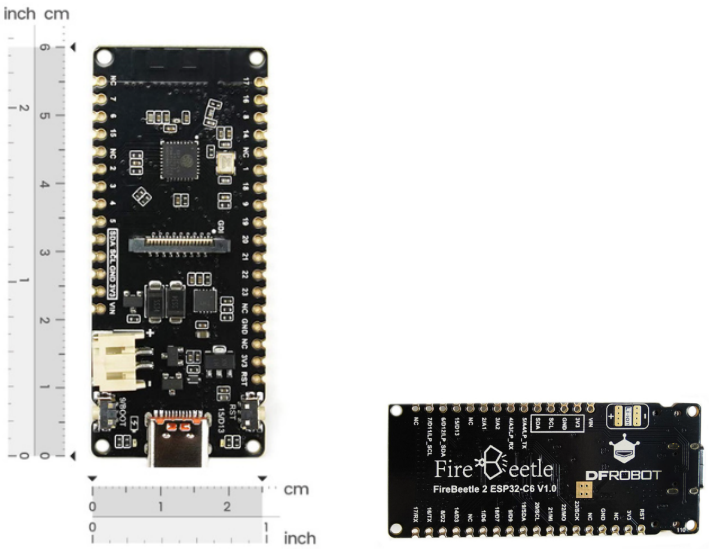

Figure 4.16: ESP32 FireBeetle C6

One of the primary reasons for selecting this board was its ultra-low power consumption, which is crucial for energy-constrained applications. According to the datasheet:

- Version 1.0: Deep sleep current of 16 ţA
- Version 1.1: Deep sleep current of 36 ţA

For more information about this board, you can refer to [20].

To verify these specifications under our specific setup, we used the Power Profiler Kit II (PPK2) to measure the actual current draw in deep sleep mode. The measured results are shown in Figure 4.17.

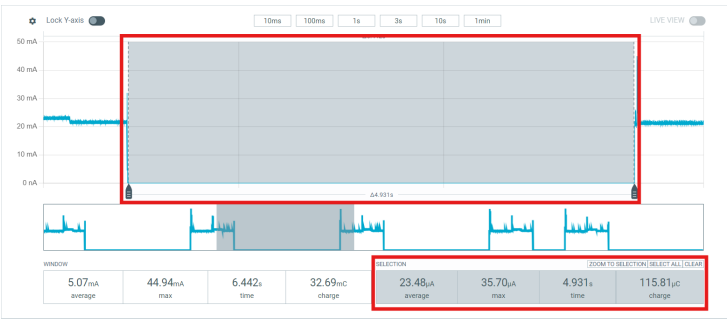

Figure 4.17: Power consumption of the ESP32 FireBeetle C6 in deep sleep mode

The ESP32 FireBeetle C6 plays a central role in managing and interfacing with other components in the system:

- **RF125 Module:** The ESP32 is used to configure the RF125 module by sending initialization and control commands (as detailed in Appendix A). It also receives and logs transmitted data to ensure proper communication before field deployment.
- **AS3933 Wake-Up Receiver:** The microcontroller processes the digital outputs of the AS3933. Specifically, when the `WAKE-UP` pin goes highindicating a successfully received WuCthe ESP32 samples the signal outputted by the `DAT` pin, using the `CL_DAT` (Manchester-recovered clock), to reconstruct the transmitted data sequence.

This integration enables the system to reliably detect wake-up events, decode incoming data, and log or respond to transmissions with minimal power usage.

4.5 DHT-22 sensor

The **DHT22**, also known as *AM2302*, shown in Figure 4.18 is a low-cost digital sensor commonly used for measuring **temperature and humidity**. It provides reliable readings within a temperature range of $-40°C$ to $+80°C$ and a humidity range of 0% to 100% relative humidity (RH). The typical accuracy is $\pm 0.5°C$ for temperature and $\pm 2-5\%$ RH for humidity.

Figure 4.18: DHT-22 sensor

The sensor communicates via a single-wire digital interface, which simplifies connection to microcontrollers such as the *ESP32*. Although its response time is relatively slow, the DHT22 is widely used due to its good balance of performance, ease of use, and affordability.

4.6 Conclusion

In this chapter, we presented the key hardware components that form the foundation of our system. The selected communication kits enable reliable magnetic induction-based data exchange at 125 kHz, while the Firebeetle ESP32-C6 microcontroller offers low-power operation suitable for IoT applications. The DHT-22 sensor provides basic environmental measurements, with the flexibility to integrate alternative sensors as needed. Together, these components offer a modular and energy-efficient platform tailored for our intended

use case. In the following chapter, we present the experimental testbed and explain how the hardware components were utilized throughout the experiments.

Chapter 5

Experimental Testbed and Implementation

5.1 Introduction

In the previous chapter, we presented the hardware components and modules used in the development of our system. This included the selection, configuration, and integration of each element to ensure proper functionality and compatibility.

In this chapter, we present the experimental part of our work. We begin by introducing the **evaluation metrics**, which define the key characteristics we aim to measure to assess the performance of our system. Next, we provide, for each experiment, an **overview of the experimental setup** using block diagrams, followed by a detailed description of the **actual hardware setup** and the methodology used to carry out the experiments. Finally, we present and discuss the **results** obtained from these experiments.

5.2 Evaluation Metrics

5.2.1 Probability of Successful Wake-Up

The *empirical probability of successful wake-up* is defined as the ratio of the number of wake-up signals that successfully trigger a response from the receiver to the total number of wake-up signals transmitted. It provides a practical measure of the reliability of the wake-up communication under specific experimental conditions.

$$P_{\text{succ}} = \frac{N_{\text{recv}}}{N_{\text{sent}}} \tag{5.1}$$

where:

- N_{recv} is the number of successful wake-up detections,
- N_{sent} is the total number of wake-up signals transmitted.

This metric is used to evaluate the performance of wake-up radio systems in real-world scenarios, accounting for environmental factors, signal attenuation, and system sensitivity.

5.2.2 BER

In digital transmission, the number of bit errors is the number of received bits of a data stream over a communication channel that have been altered due to noise, interference, distortion or bit synchronization errors.

BER is defined as the total count of error bits to the total count of transmitted bits from sender to receiver. This Quality of Service (QoS) metric lies at the physical layer where data is in the form of bits. The formula of BER is :

$$\text{BER} = \frac{Bits_{error}}{Bits_{transmitted}} \tag{5.2}$$

where:

- $Bits_{error}$ is the total count of error bits.
- $Bits_{transmitted}$ is the total count of transmitted bits.

5.2.3 Battery Lifetime

The *battery lifetime* refers to the total duration during which a system can operate on a given battery before complete depletion. It depends on the average current consumption of the system, the battery capacity, and the duty cycle of system components such as the wake-up receiver and the main transceiver. It is a key metric for evaluating the energy efficiency and long-term deployment feasibility of low-power wireless systems.

$$T_{\text{life}} = \frac{C_{\text{bat}}}{I_{\text{avg}}} \tag{5.3}$$

where:

- C_{bat} is the battery capacity (in mAh),
- I_{avg} is the average current consumption of the system (in mA).

Since we have two modes *active mode* and *sleep mode*:

- **Active mode:**
  - Time per cycle: T_{active}
  - Current: I_{active}
- **Sleep mode:**
  - Time per cycle: T_{sleep}
  - Current: I_{sleep}

Then the **average current** is:

$$I_{\text{avg}} = \frac{T_{\text{active}} \cdot I_{\text{active}} + T_{\text{sleep}} \cdot I_{\text{sleep}}}{T_{\text{active}} + T_{\text{sleep}}} \tag{5.4}$$

Since we want a system that lasts long and consumes very little power, we convert the battery capacity to [mA · year] by multiplying it by $\frac{1}{24 \times 365.25} = \frac{1}{8766}$.
The final expression for the *Battery Lifetime* in Year is:

$$T_{\text{life}}[\text{Year}] = \frac{C_{\text{bat}}[\text{mA} \cdot \text{Year}]}{I_{\text{avg}}[\text{mA}]} \tag{5.5}$$

5.3 Experimental Testbed and System Evaluation

All experiments were conducted in a sandy medium, as the study was carried out in a region of Saudi Arabia where sand was the predominant and only available soil type.

Due to the limited ability to dig deeply and following the methodology adopted in previous testbeds, the first two experiments were conducted with both the transmitter and receiver buried at the same depth (0.8 m). The horizontal distance between them was gradually increased, starting from 0mt, in increments of 0.5 m $\pm$ 0.1 m, until communication was no longer established.

In the experiment 3 we tested the whole system including the wake-up call, the sensing and the data transmission at a depth of 0.8m.

5.3.1 Experiment 1: Probabilty of Successful Wake-Up

The objective of this experiment is to evaluate the number of successfully received wake-up calls relative to the number of transmitted ones, as a function of distance. The corresponding block diagram is shown in Figure 5.1.

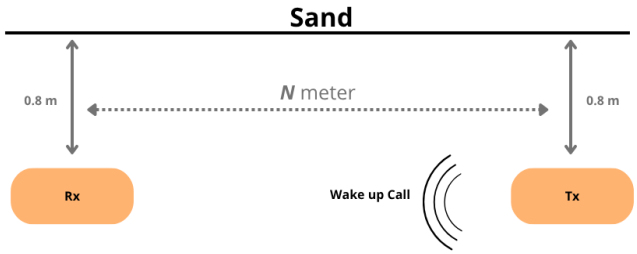

Figure 5.1: Block diagram for the experiment 1

For these measurements we used the AS3933 125 kHz Wake-up Transmitter Board shown in Figure 4.14 as a transmitter and the AS3933 demoboard 4.13 as receiver since there was no need to transmit customized data.

Before explaining the measurement procedure, let us briefly describe how a wake-up call (WuC) is detected. When the receiver's enabled antenna detects the predefined pattern configured in the settingsspecifically, a 16-bit pattern 0x9669 (0b1001011001101001)in our casethe wake-up pin outputs a high pulse lasting 1 second, as illustrated in Figure 5.2.

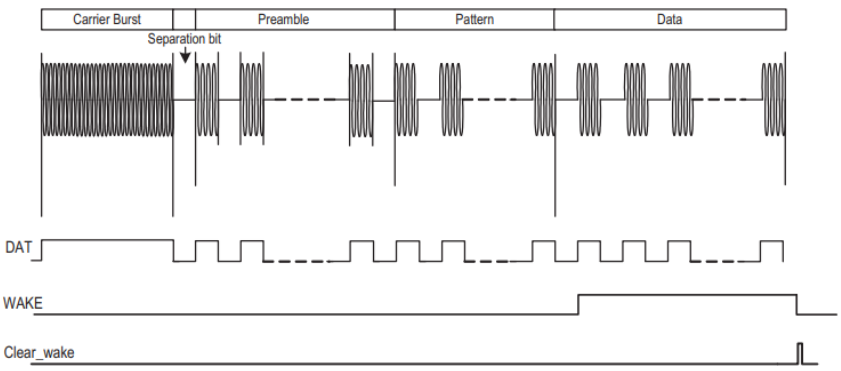

Figure 5.2: AS3933 communication protocol

To evaluate the probability of successful wake-up detection, we press the *AUTO* button, which triggers the transmission of a wake-up call composed of a *carrier, preamble, and pattern*. Ideally, one WuC should be transmitted every second, resulting in 60 transmissions per minute. However, oscilloscope analysis revealed that the actual time interval between two consecutive transmissions is approximately 1.048 seconds, corresponding to **57 WuCs per minute**.

So for each distance, we keep sending WuC for 6 minutes, therefore we have 342 WuC sent. We program the Firebeetle ESP32 C-6 to count how many WuC are received, and we do the ratio of the number of successful wake-up detections over the total number of

wake-up signals transmitted as shown in Equation 5.1.

In the actual setup, we soldered long wires to the transmitter's buttons to allow remote control from the ground surface. The transmitter was powered using a 12 V battery. To protect it from sand, we placed the transmitter inside a plastic box, which was then sealed in a plastic bag. Figure 5.3 illustrates the transmitter setup used in this experiment.

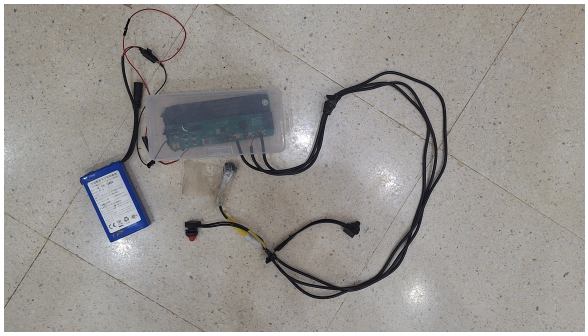

(a) The transmitter boxed and powered

(b) The transmitter protected and buried

Figure 5.3: Transmitter's set-up for experiments 1 and 2

The receiver (Rx) was powered by a 3 V coin cell and connected to the ESP32 Fire-Beetle C6, which was programmed to record the number of successful WuC events. The ESP32 was powered by a 3.7 V Li-Po battery. This underground portion of the receiver setup is shown in Subfigure 5.4a.

For convenience, the ESP32 was programmed to compute the probability of successful wake-up when one of its digital pins is connected to ground (0 V), and to calculate the BERin Experiment 2when the pin is connected to Vcc (3.3 V).

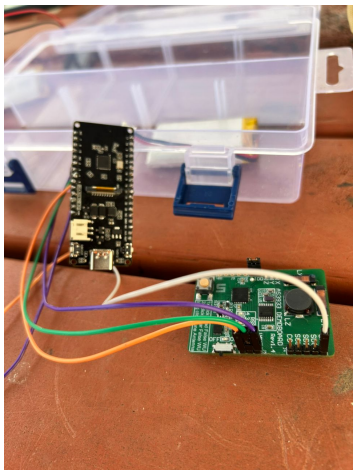

(a) Underground part of the receiver setup

(b) Surface part of the receiver setup

Figure 5.4: Receiver setup: underground and surface components

To enable this functionality, long jumper wires were connected to the receiver. The blue jumper wire, visible in Subfigure 5.4b, was specifically used to control the logic level input for switching between WuC probability measurement and BER evaluation. A

second ESP32, positioned at the ground surface, acted as a DC-DC converter to supply the 3.3 V required for the BER measurement. This surface component is also shown in Subfigure 5.4b.

To protect the receiver from sand, the underground components were placed in a protective box, as shown in Subfigure 5.5a. The complete receiver setup, including the buried state, is shown in Figure 5.5.

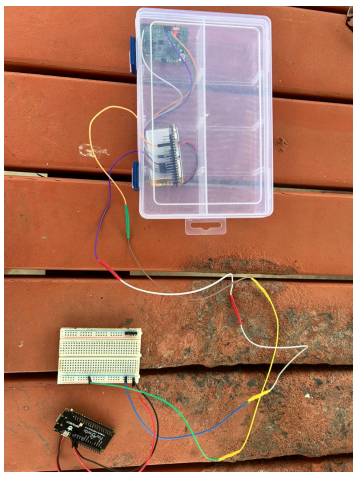

(a) Boxed underground and surface components of the receiver setup

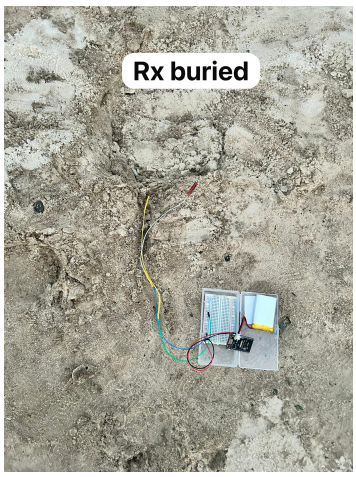

(b) Receiver setup after burying the underground part

Figure 5.5: Complete receiver setup with protection and burial

The whole set-up for the experiment is shown in Figure 5.6

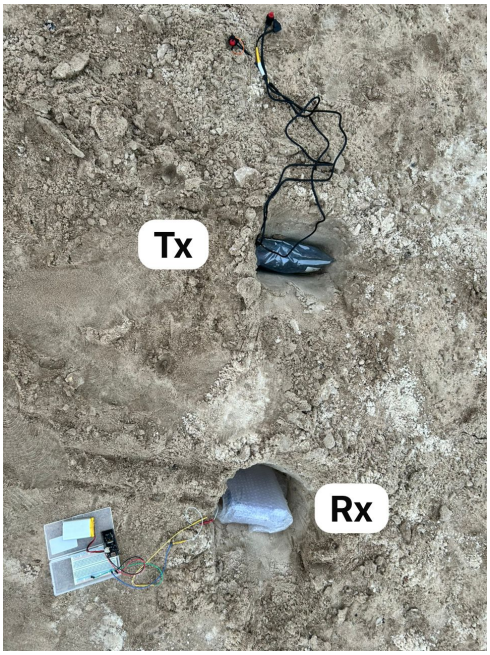

Figure 5.6: The set-up for the experiment 1

After fine-tuning the parameters, a symbol rate of 512 symbols/second was found to be the most suitable for reliable long-range transmission, particularly due to the challenging underground environment.
The configuration settings used for the receiver are shown in Figure 5.7.

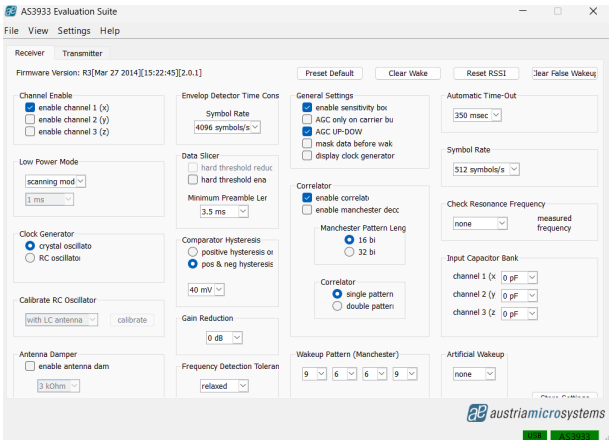

Figure 5.7: Setting of the receiver for the probability of successful wake-up measurements

5.3.2 Experiment 2: BER

The objective of this experiment is to measure the Bit Error Rate (BER), as defined in Equation 5.2, with respect to distance. The experimental setup is illustrated in the block diagram shown in Figure 5.8.

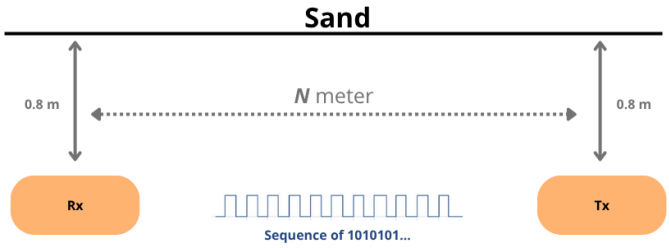

Figure 5.8: Block diagram of Experiment 2

The fine-tuned parameters used in this experiment are identical to those in Experiment 1 and are shown in Figure 5.7.

In our system, pressing the `PATTERN + DATA` button triggers the transmission of a repeating bit sequence 101010 . . . for a duration of one second. With the selected symbol rate, 182 bits are received during this period.

By enabling *Manchester decoding* in the receiver configuration, we obtain both the received data and the recovered Manchester clock. This clock is used to sample the incoming bits and compare them with the expected 101010 . . . pattern.

Referring to the communication protocol illustrated in Figure 5.2 and the oscilloscope capture in Figure 5.9, we observe that the data sequence is transmitted during the wake-up pulse. The recovered Manchester clock enables accurate sampling, and according to the AS3933 datasheet (Appendix C), data should be sampled on the rising edge of this clock.

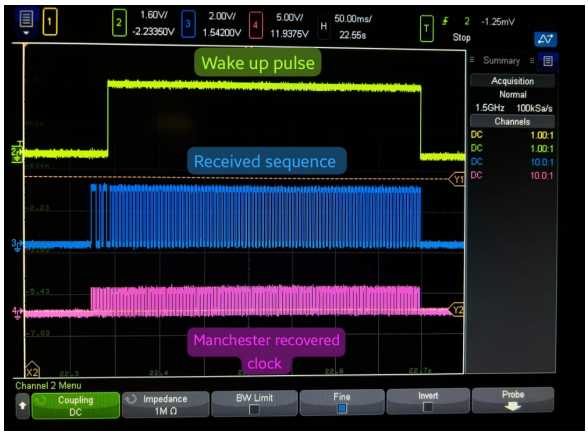

(a) Wake-up pulse, received data, and recovered Manchester clock

(b) Zoomed view of the received bit sequence and recovered clock

Figure 5.9: Oscilloscope analysis of the receiver output

Since the transmitted bit sequence is known, we developed a script to sample the received data on the rising edges of the Manchester-recovered clock and compare it to the expected pattern. The Bit Error Rate (BER) is then calculated using Equation 5.2, as the ratio of the number of erroneous bits to the total number of transmitted bits.

To improve reliability, each measurement was repeated 10 times at every tested distance, and the resulting BER values were averaged.

Regarding the experimental setup, the ESP32 was programmed to compute either the probability of successful wake-up or the BER, depending on the logic level applied to a designated digital pin. When connected to 0 V, it computes the wake-up probability; when connected to 3.3 V, it computes the BER. For the BER evaluation, the pin was connected to 3.3 V via the blue jumper wire, which is visible in Subfigure 5.4b. This surface part of the setup is responsible for powering the ESP32 and providing the necessary logic control. **This was the only modification to the setup between Experiment 1 and Experiment 2.**

5.3.3 Experiment 3: Testing the Whole System

In this experiment, we aim to evaluate the end-to-end functionality of the system, including both the wake-up call mechanism and the data transmission process. Due to the absence of a UAV, the tests were carried out using only the above-ground node, while the underground node was buried at a depth of 0.8 m. The block diagram of the experimental setup is shown in Figure 5.10.

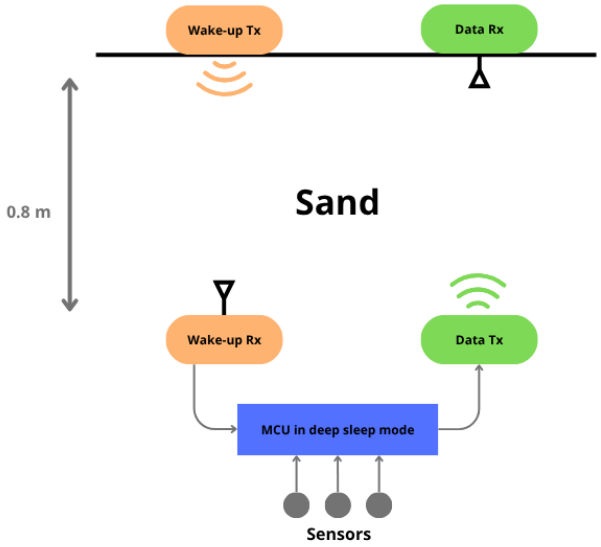

Figure 5.10: Block diagram of the whole system used in Experiment 3

As shown in Figure 5.10, the system is divided into two parts: the surface node and the underground node.

The surface part of the system, shown in Subfigure 5.11a, includes two main components: the AS3933 transmitter, powered by a 12 V battery, which is responsible for sending the wake-up signal; and an AS3933 demo board configured as a data receiver, powered by a 3 V coin cell battery. To initiate the communication process during the experiment, we simply press the "Pattern" button on the wake-up transmitter, which sends a wake-up call to the underground receiver, activating the buried node.

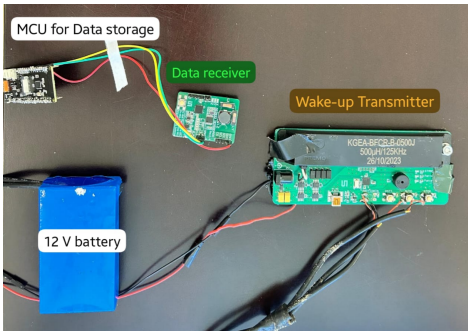

(a) Above-ground part of the whole system

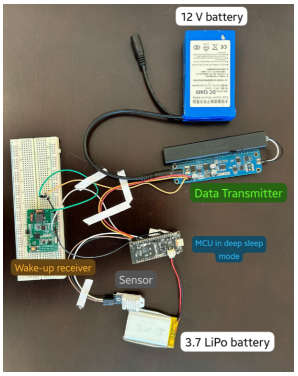

(b) Underground part of the whole system

Figure 5.11: Experimental setup of the complete system

The underground part of the system, shown in Subfigure 5.11b, consists of an AS3933 receiver powered by a 3 V coin cell battery. Upon detecting the wake-up call, the receiver triggers the Microcontroller Unit (MCU) to wake from deep sleep mode. The MCU is connected to a DHT-22 sensor and is programmed to record environmental data (temperature and humidity). Once the sensing process is complete, the MCU sends a

command to the RF125 transmitter, instructing it to wirelessly transmit the collected data to the above-ground AS3933 data receiver.

The complete experimental setup, including both surface and underground components, is illustrated in Figure 5.11.

Since the system includes two transmitters and two receivers, they must operate at different symbol rates to avoid interference. For data transmission, the symbol rate was determined by the RF125 module, which transmits at 1024 symbols/sec. For the wake-up calls, we used a lower symbol rate of 512 symbols/sec. All other configuration settings remained the same as in the previous experiments (see Figure 5.7).

After assembling both parts of the system, we enclosed the underground components in a plastic box and wrapped it with plastic film to prevent sand infiltration. Figure 5.12 illustrates the experimental setup during the tests.

(a) The above ground part during the experiments

(b) The underground part protected and buried

Figure 5.12: The experimental set-up during experiments

Before deploying the full system underground, we conducted preliminary indoor testing. The ambient conditions during the test were a temperature of 26 °C and a relative humidity of 60%. The sensed data were successfully received, with the temperature encoded in Byte 0 and the humidity in Byte 1. An additional checksum byte is included in the RF125 Tx communication protocol to verify the integrity of the received data. The results of these indoor experiments are presented in Figure 5.13.

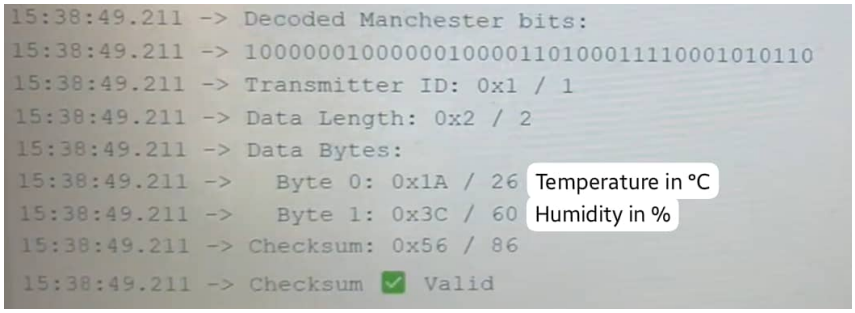

Figure 5.13: the result of the indoor experiments

5.3.4 Battery Lifetime

Since we are interested especially in the power consumption of the buried devices, we evaluated the power consumption of the RF125 Tx and the AS3933 receiver.

To characterize their power consumption, we employed the Nordic Semiconductor PPK2,*described in Appendix B*, in `Ampermeter mode`.

In this configuration, the transmitter/receiver board was powered by an external power supply, while the PPK2 was connected in series with the power line to measure the current drawn by the device under test Device Under Test (DUT). This setup allowed us to non-invasively monitor the transmitters current consumption without supplying power through the PPK2 itself. The PPK2 captured real-time current measurements with high resolution and accuracy, ranging from 200 nA to 1 A, and streamed the data to the nRF Connect for Desktop - Power Profiler application. This enabled detailed visualization and analysis of the transmitter's/receiver's current profile during wake-up signal transmission, including peak current, average consumption, and idle state behavior.

To estimate the battery lifetime, we considered different battery capacities and varied the number of transmissions per hour.
We analyzed two distinct scenarios:

- **Scenario 1:** The transmitter remains powered on at all times, even when not actively transmitting.
- **Scenario 2:** The transmitter is completely turned off when not transmitting.

In this context, the term *sleep* has two different meanings:

- In **Scenario 1**, *sleep* refers to the standby mode while the transmitter remains powered on (see Table 5.1).
- In **Scenario 2**, *sleep* refers to the transmitter being entirely powered off (see Table 5.2).

The only parameter that changes between the two scenarios is the transmitter's sleep current I_{sleep}.

Table 5.1: Operating parameters and average current for the RF125 Transmitter and AS3933 Receiver in scenario 1

Parameter	**RF125 Transmitter**	**AS3933 Receiver**
T_{active} (ms)	variable	variable
I_{active} (mA)	494.56	$6.66 \cdot 10^{-3}$
T_{sleep} (ms)	variable	variable
I_{sleep} (μA)	2.9	$6.44 \cdot 10^{-3}$
I_{avg} (mA)	variable	variable

Table 5.2: Operating parameters and average current for the RF125 Transmitter and AS3933 Receiver in scenario 2

Parameter	**RF125 Transmitter**	**AS3933 Receiver**
T_{active} (ms)	variable	variable
I_{active} (mA)	494.56	$6.66 \cdot 10^{-3}$
T_{sleep} (ms)	variable	variable
I_{sleep} (μA)	0	$6.44 \cdot 10^{-3}$
I_{avg} (mA)	variable	variable

5.4 Results and Discussion

5.4.1 Experiment 1: Probability of Successful Wake-Up

Figure 5.14 illustrates the success rate of wake-up calls as a function of distance, with measurements taken from 0.5 to 8 meters. It is evident that up to approximately 6.8 meters, the system consistently receives all wake-up calls with a 100% success rate. However, beyond this threshold, the performance begins to degrade significantly. The success rate drops sharply between 6.8 and 7.7 meters, and at around 7.7 meters, no wake-up calls are received, indicating a complete loss of wake-up capability at that range.

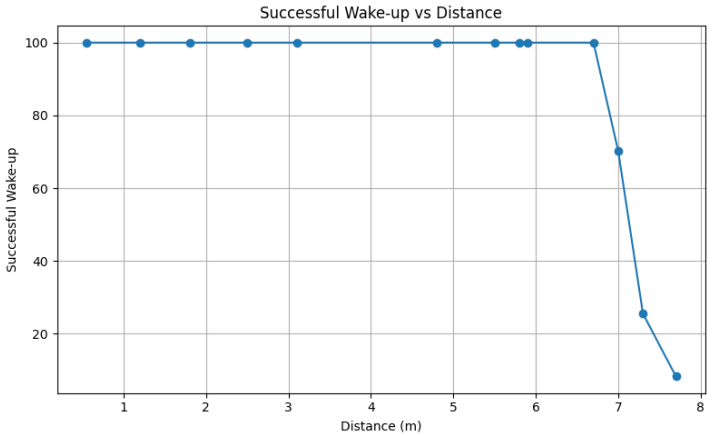

Figure 5.14: Empirical Probability of successful wake-up VS distance

5.4.2 Experiment 2: BER

The results of the BER versus the distance between the transmitter and the receiver are summarized in Figure 5.15. The BER remains at zero up to approximately 3.8 meters, indicating error-free communication within this range. Beyond this point, the BER increases as the signal quality deteriorates with distance, resulting in bit errors. At greater distances, the BER drops back to zeronot due to improved transmission, but because the receiver fails to detect any data, indicating a complete loss of communication. Interestingly, the wake-up callcomprising a carrier, preamble, and a fixed 16-bit patternwas

successfully received up to 6.8 meters. This suggests that short, well-defined transmissions are more robust against channel impairments. We hypothesize that this is due to the increased reliability of synchronization and detection mechanisms for short, known sequences with minimal duration. Consequently, the range could potentially be improved by transmitting shorter data packets. However, this hypothesis requires further validation through additional experiments.

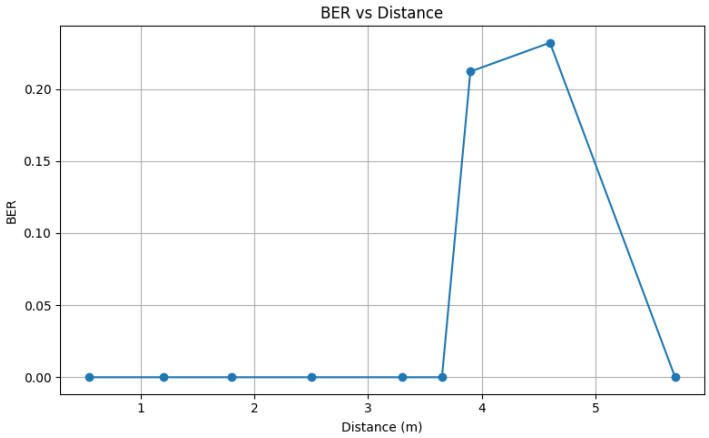

Figure 5.15: BER VS the distance between the transmitter and the receiver

5.4.3 Experiment 3: Testing the whole sytem

Figure 5.16 shows the successful decoding of a data signal transmitted from the underground node to the aboveground receiver. The signal was Manchester encoded, meaning each bit is represented by a transition, and decoding had to be performed without a recovered clock based only on the timing and polarity of signal edges. The decoded Manchester bitstream is clearly shown, and from it, the structure of the transmitted frame is reconstructed. The transmitter ID is correctly identified as 0x1, the data length is 0x2 (2 bytes), and the received data bytes are 0x1F and 0x50. These correspond to a temperature value of 31°C and a humidity value of 80%, respectively. The relatively high humidity value is consistent with the presence of water content in the sand.

```
17:09:35.124 -> HIGH for 1015 us   → '0'
17:09:35.124 ->
17:09:35.124 -> HIGH for 1015 us
17:09:35.124 -> LOW  for 504 us   → '1'
17:09:35.124 ->
17:09:35.124 -> HIGH for 499 us
17:09:35.124 -> LOW  for 501 us   → '1'
17:09:35.124 ->
17:09:35.124 -> HIGH for 503 us
17:09:35.124 -> LOW  for 480 us   → '1'
17:09:35.124 ->
17:09:35.124 -> HIGH for 516 us
17:09:35.124 -> LOW  for 315989 us
17:09:35.124 -> Decoded Manchester bits:
17:09:35.124 -> 10000001000000100001111101010000110111
17:09:35.124 -> Transmitter ID: 0x1 / 1
17:09:35.124 -> Data Length: 0x2 / 2
17:09:35.124 -> Data Bytes:
17:09:35.124 ->   Byte 0: 0x1F / 31
17:09:35.124 ->   Byte 1: 0x50 / 80
```

Figure 5.16: Successful Decoding of an Underground-to-Aboveground Data Transmission

5.4.4 Battery Lifetime

Battery Lifetime of the AS3933 Receiver

We have calculated the battery lifetime of the AS3933 receiver for varying numbers of receptions per hour and different battery capacities. As shown in Figure 5.17, changing the number of receptions per hour has a minimal effect on the overall battery lifetime. This is because the AS3933 is an ultra-low-power device, and the difference in power consumption between its idle and active (receiving) states is very small. Therefore, increasing the frequency of receptions has a negligible impact on the total energy consumed.

From the figure, we can also observe that even a battery with a capacity of 220mAh allows the receiver to operate for more than three years. With a 540mAh battery, the lifetime exceeds 9 years, and with a 1000mAh battery, it reaches approximately 17 years. These results demonstrate that only a small battery is needed to ensure long-term underground operation of the receiver, making the system both efficient and practical for remote sensing applications.

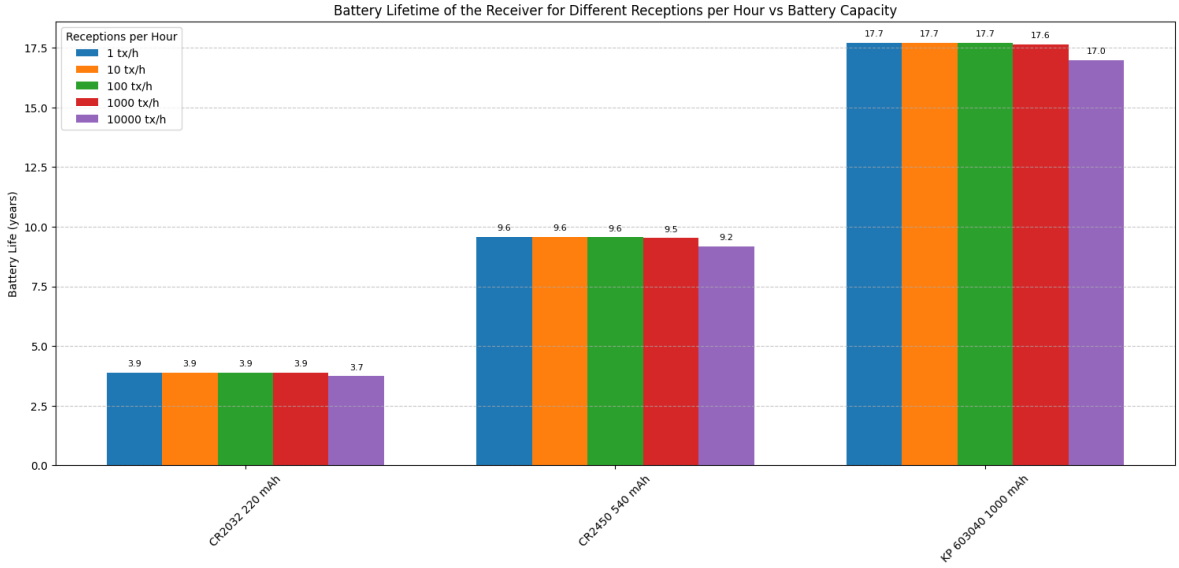

Figure 5.17: Battery Lifetime of the AS3933 Receiver

Battery Lifetime of the RF125 Tx Transmitter

Figure 5.18 presents the case where the transmitter remains on continuously, even when not transmitting, while Figure 5.19 shows the estimated battery lifetime of the RF125 Tx transmitter when it is turned off during idle periods (i.e., when not transmitting).

As illustrated in Figure 5.18, keeping the transmitter powered on at all times significantly increases power consumption. Even with a high-capacity 9000mAh battery, the system fails to reach half a year of operation, underscoring the inefficiency of this approach.

To address this issue, we propose powering the transmitter using a MOSFET that acts as a switch. The gate of the MOSFET is connected to the wake-up pin, which outputs a high level when a WuC is received. Upon receiving this signal, the MOSFET turns on, connecting the transmitter directly to the battery and enabling transmission. When

no WuC is received, the MOSFET remains off, disconnecting the transmitter from the battery and eliminating power consumption during idle periods. Since MOSFETs consume negligible power at the gate (especially for static signals and low switching frequencies), this solution introduces no significant overhead to the system's power budget.

This strategy yields significantly improved lifetimes, as shown in Figure 5.19. With only one transmission per hour, the battery lifetime reaches approximately 75 years for a 4800mAh battery, 107 years for 6800mAh, and 141 years for 9000mAh. These results clearly demonstrate the effectiveness of switching off the transmitter during idle periods to maximize battery efficiency. However, as the number of transmissions increases, the lifetime decreases notably. At nine transmissions per hour, the lifetime drops to 8 years for 4800mAh, 11 years for 6800mAh, and 15 years for 9000mAh.

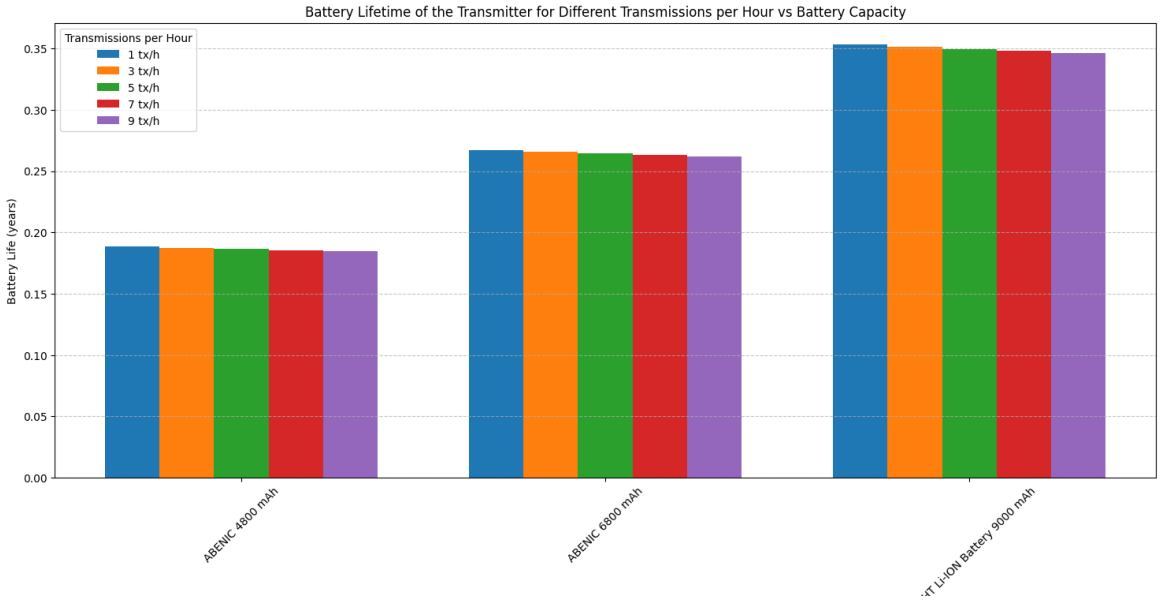

Figure 5.18: Battery Lifetime of the RF125 Tx Transmitter in Scenario 1 (keeping it on when not transmitting)

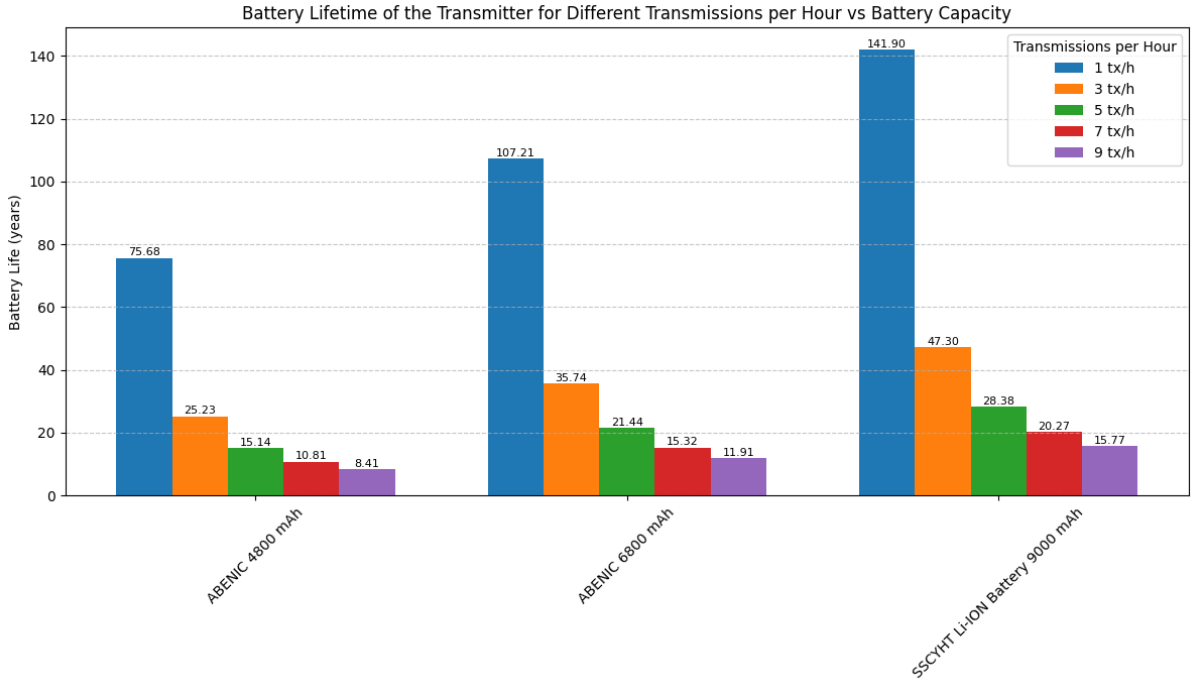

Figure 5.19: Battery Lifetime of the RF125 Tx Transmitter in Scenario 2 (completely turned off when not transmitting)

From these calculations, we can draw two key conclusions:

- First, the most effective way to reduce power consumption is to keep the transmitter turned off when no data is being sent. This significantly extends the battery life by eliminating unnecessary energy drain during idle periods.
- Second, the number of transmissions per hour should be carefully selected based on the desired operational lifetime of the transmitter. Increasing the transmission frequency shortens battery life, which in turn increases the need for battery replacements or recharging a critical consideration for long-term or hard-to-access deployments.

5.5 Conclusion

In this chapter, we presented the experiments we conducted to evaluate the performance of our system. Our tests were designed to verify its functional reliability and assess its energy efficiency in realistic scenarios.

The results showed that the system operates correctly and is highly power-efficient, especially when the transmitter is kept off during idle periods. By activating the transmitter only when a transmission is required, we were able to achieve very long battery lifetimes making the solution suitable for long-term deployments with minimal maintenance.

In terms of communication range, we observed successful wake-up call detection up to 6.8 meters, which is promising. However, reliable data transmission, as measured by the bit error rate (BER), was limited to approximately 3.8 meters. We believe this can be improved by optimizing the transmitted data format in particular, by sending smaller data packets, which may be less susceptible to channel impairments.

In the next chapter, we will study the large-scale model of our system in order to evaluate its behavior and performance in more complex deployment scenarios.

Chapter 6

Large-Scale Network Analysis

6.1 Introduction

As underground communication systems scale up, understanding their behavior in large deployments becomes crucial for assessing performance, reliability, and feasibility. This chapter focuses on the analysis of large-scale magnetic induction underground to above-ground networks, where multiple transmitters and receivers may operate simultaneously in complex environments.

6.2 Motivation and Use of Stochastic Geometry

In the context of underground wireless communication, especially with magnetic induction (MI) as the chosen technique, it is essential to understand and quantify system performance under realistic, large-scale deployment scenarios. One critical aspect of our study is the reliability of wake-up signal transmission to buried receivers, which is influenced by factors such as the spatial distribution of transmitters and signal propagation constraints. To address this, we employed stochastic geometry as a powerful mathematical framework to model the random spatial placement of nodes and analytically derive key performance metrics such as the probability of successful and false wake-ups. This approach allowed us to capture the inherent randomness in real-world deployments and obtain generalizable insights beyond specific experimental setups. To validate our analytical model, we conducted extensive Monte Carlo simulations, which showed a strong agreement with the stochastic geometry predictions. This dual approach not only reinforced the robustness of our theoretical analysis but also provided a solid foundation for optimizing network design and understanding system limits in realistic conditions.

6.3 System Modeling with SG

6.3.1 Description

We consider a wireless underground sensor network where underground nodes aim to communicate with above-ground nodes. The above-ground nodes (black triangles in 6.1) are spatially distributed according to a homogeneousPoisson Point Process (PPP) Φ with intensity λ (nodes/m^2) on the two-dimensional plane. These nodes partition the plane into Voronoi cells (shown in blue dashed lines), each corresponding to the coverage area of an above-ground node.

An underground node, shown as a blue dot in 6.1, lies at a fixed depth H and is projected onto the 2D plane for analysis. The underground node communicates with its nearest above-ground anchor node, located at a horizontal distance R. The red dashed circles represent other above-ground nodes at greater distances. The total 3D Euclidean distance to this nearest node is given by:

$$d = \sqrt{R^2 + H^2} \tag{6.1}$$

This study aims to determine the probability of successful wake-up and the probability of false wake-up for an underground node communicating with above-ground nodes. Two approaches are used:

- A **Monte Carlo simulation-based method**, where numerous random realizations of the above-ground network are generated according to aPPP.

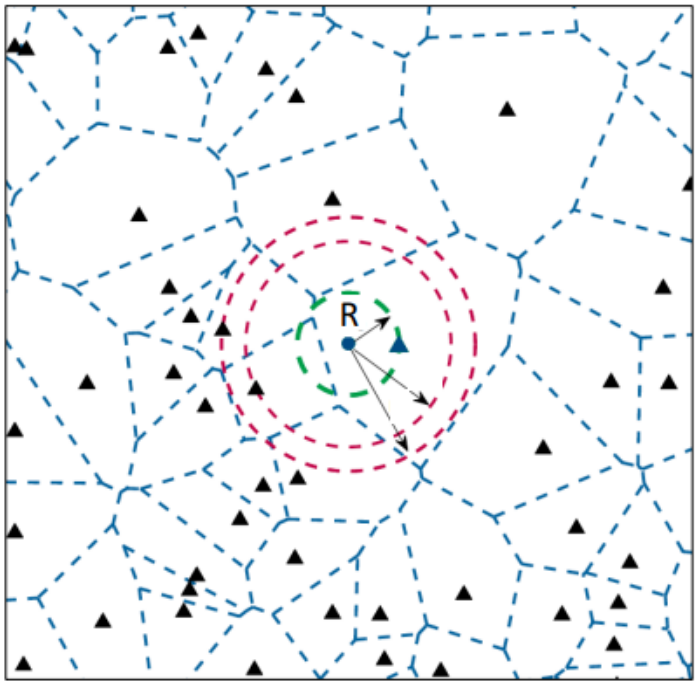

Figure 6.1: Illustration of the System Model

- A **stochastic geometry-based analysis**, where we mathematically derive expressions for the desired probabilities using properties of the PPP.

The results obtained from both approaches are then compared to ensure consistency and validate the theoretical model.

6.3.2 Probability of Successful Wake-up

The probability of successful wake-up is defined as the probability that the total received power from all above-ground nodes, denoted P^T, exceeds a given threshold τ. Mathematically, this is expressed as:

$$\mathbb{P}_s = \mathbb{P}(P^T > \tau) \tag{6.2}$$

6.3.3 Probability of False Wake-up

The probability of successful wake-up is defined as the probability that the interferencei.e., the total received power from all the above-ground nodes except the nearest one, denoted $\mathbb{I}$ is great than a certain threshold γ. This event corresponds to the underground node being erroneously triggered by interference rather than by its intended nearest node. Mathematically, this is expressed as:

$$\mathbb{P}_f = \mathbb{P}(I > \gamma) \tag{6.3}$$

6.4 Monte Carlo Simulations

6.4.1 Description of the Steps of the Simulation

To evaluate the performance of our system, we conduct a Monte Carlo simulation to estimate the probabilities of successful and false wake-up events. The methodology proceeds as follows:

- The simulation region is a square area of $100 \times 100\,\mathrm{m}^2$ centered at the origin, within which above-ground nodes are deployed according to a homogeneous PPPwith intensity $\lambda = 0.01\,\mathrm{nodes/m}^2$.
- In each iteration, the number of above-ground nodes is drawn from a Poisson distribution with mean λA, where A is the area of the region. Their positions are sampled uniformly within the region.
- An underground node is placed at the origin with a fixed depth $H = 10\,\mathrm{m}$. The 3D Euclidean distance to each above-ground node is calculated as:

$$d_i = \sqrt{R_i^2 + H^2} \tag{6.4}$$

  Where R_i is the horizontal distance from the underground node to each above-ground node.
- The received power from each above-ground node is computed using the magnetic induction channel model shown in Equation 3.15.
- Table 6.1 shows the values of the different constants used in this simulation.

Table 6.1: Simulation Parameters for Monte Carlo Evaluation

Parameter	**Value**	**Description**
U_s	$1\,\mathrm{V}$	Source voltage
$R_t = R_r$	$1\,\Omega$	Coil resistances
L_t	$0.5\,\mathrm{mH}$	Inductance of transmitting coil
L_r	$7.2\,\mathrm{mH}$	Inductance of receiving coil
f	$125\,\mathrm{kHz}$	Operating frequency
ω	$2\pi \cdot 125 \cdot 10^3\,\mathrm{rad/s}$	Angular frequency
α	90°	Angle between the axes of the coils
H	$10\,\mathrm{m}$	Depth of underground node
λ	$0.01\,\mathrm{nodes/m}^2$	PPP intensity of above-ground nodes
Area	$100 \times 100\,\mathrm{m}^2$	Simulation region
Iterations	10^4	Number of Monte Carlo simulations

- The serving above-ground node is identified as the one with the minimum 3D distance to the underground node. The total received power from all above-ground nodes is recorded as the *wake-up signal*, while the sum of the received powers from all other (non-serving) nodes is considered *interference*.
- This process is repeated for 10^4 iterations for a range of thresholds $\tau \in [-70, -68, \ldots, 20]\,\mathrm{dB}$

- The empirical probabilities are computed as:

$$\mathbb{P}_s = \frac{\text{Number of wake-up signals } > \tau}{\text{Total iterations}}, \tag{6.5}$$

$$\mathbb{P}_f = \frac{\text{Number of interference values } > \tau}{\text{Total iterations}}. \tag{6.6}$$

6.4.2 Simulation Results

The results of the Monte Carlo simulations are presented in Figures 6.2 and 6.3, which illustrate the probability of successful wake-up and false wake-up, respectively.

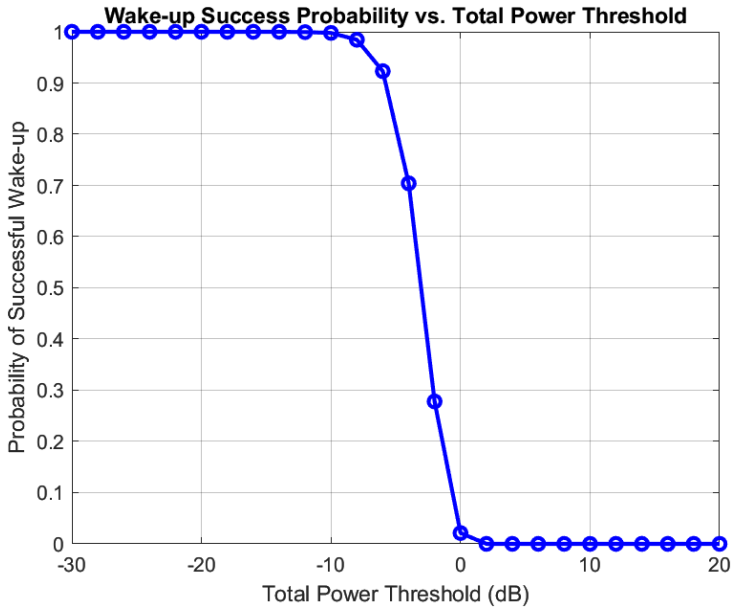

Figure 6.2: Probability of Successful Wake-up vs. Received Power Threshold (dB)

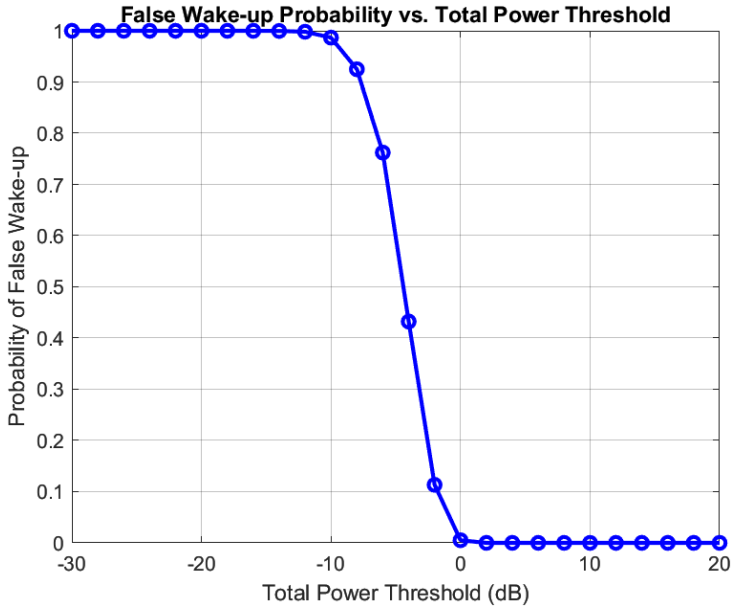

Figure 6.3: Probability of False Wake-up vs. Received Power Threshold (dB)

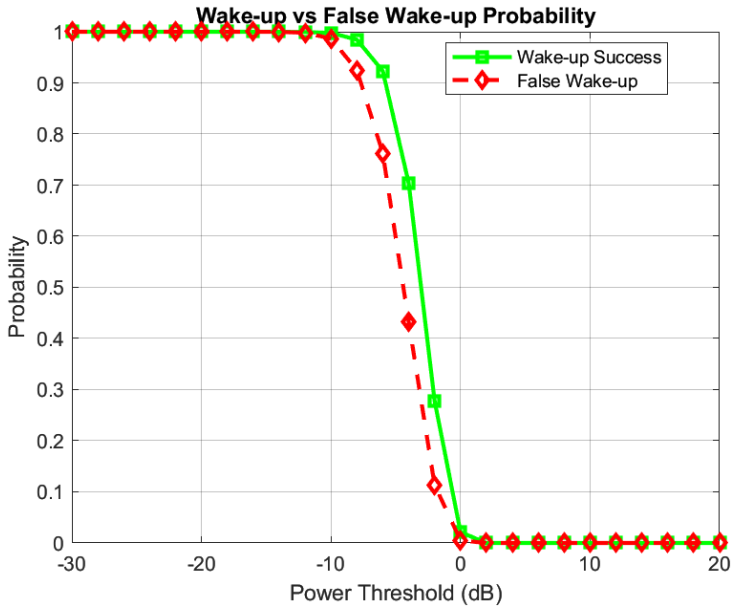

Figure 6.4: Probability of Successful and False Wake-up vs. Received Power Threshold (dB)

6.4.3 Interpretation of the Results

From Figure 6.2, we can observe the following:

- For thresholds below $-10, \text{dB}$, the probability of successful wake-up is close to 1, indicating that the wake-up signal is reliably detected by the receiver.
- Between $-10, \text{dB}$ and $0, \text{dB}$, there is a sharp decline in the success probability.
- For thresholds above $0, \text{dB}$, the probability of successful wake-up approaches zero.

A similar trend is observed in Figure 6.3 for the probability of false wake-up. Furthermore, Figure 6.4 shows that the probabilities of successful and false wake-up are very close, which is expected. Indeed, the probability of false wake-up corresponds to the probability of total received power exceeding the threshold without being due to the intended base stationi.e., the successful wake-up probability minus the contribution from the closest transmitter.

6.4.4 Effect of the Number of Turns N and Radii of the Coils a

Figures 6.5, 6.6, 6.7, and 6.8 illustrate the impact of varying the number of turns N and the coil radius a. As shown in Figure 6.5 increasing N enhances the probability of successful wake-up. However, as shown in Figure 6.7 this enhancement also leads to a higher probability of false wake-ups, reflecting an increased risk of unintentionally activating untriggered nodes. At the same time, Figure 6.6 shows that increasing the radius a decreases the system's ability to detect a WuC just like we've seen in Section 3.3. At the same time, as indicated in Figure 6.8, this effect extends to the probability of false wake-ups as well where larger coil radii reduce both successful and false wake-up probabilities.

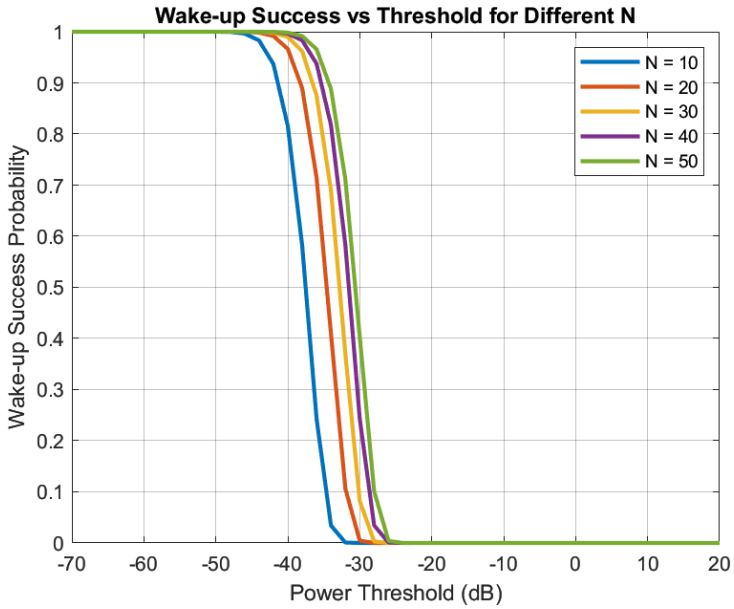

Figure 6.5: Wake-up Success Probability vs. Received Power Threshold for Different Values of N

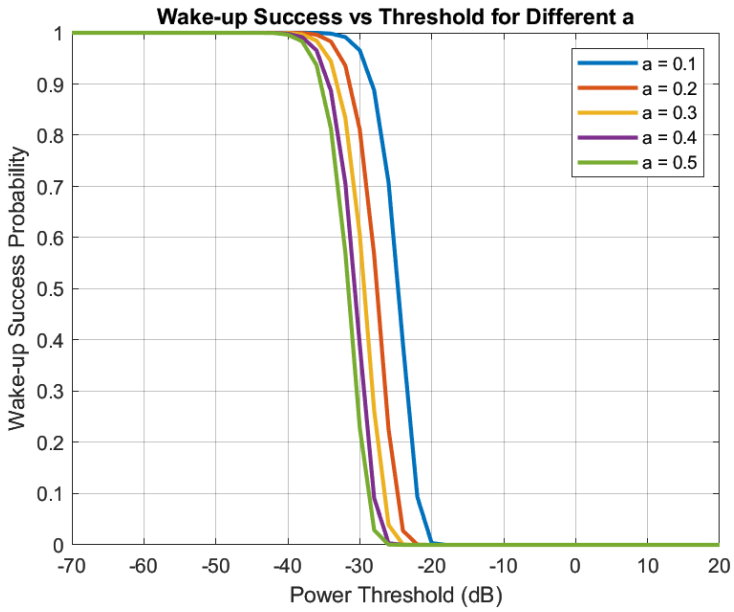

Figure 6.6: Wake-up Success Probability vs. Received Power Threshold for Different Values of a

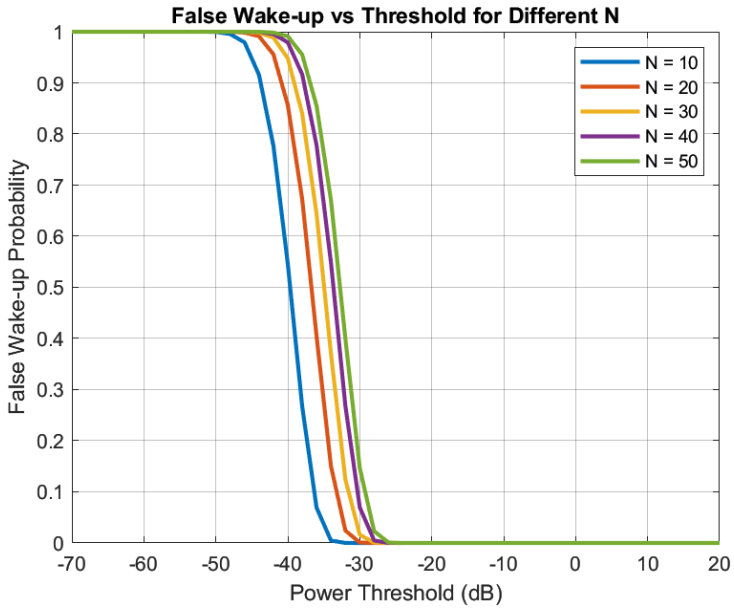

Figure 6.7: Probability of False Wake-Up vs. Received Power Threshold for Different Values of N

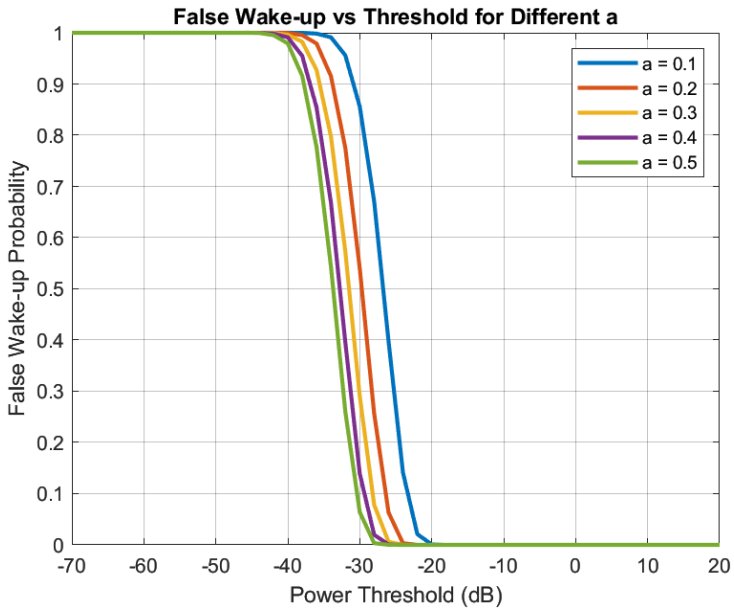

Figure 6.8: Probability of False Wake-Up vs. Received Power Threshold for Different Values of a

6.5 Analytical study

In the following we'll be deriving analytical expressions for the probabilities of successful and false wake-up.

6.5.1 Probability of Successful Wake-Up

- We want to ensure that the total received power at a node exceeds a predefined threshold τ in order to guarantee a successful wake-up. This condition can be

mathematically written as shown in equation 6.2

- If the cumulative distribution function (CDF) of the total received power P_r^T, denoted by $F_{P_r^T}(\cdot)$, is known, then this probability can be expressed as:

$$\mathbb{P}(P_r^T > \tau) = 1 - F_{P_r^T}(\tau) \tag{6.7}$$

- To gain insight into the statistical behavior of the total received power P_r^T, we conducted Monte Carlo simulations using MATLAB. Specifically, we generated 10,000 realizations of P_r^T under the given network conditions.

- The resulting values were used to plot a histogram representing the empirical distribution of the total received power. To approximate this distribution with a known theoretical model, we employed MATLABs `distfit` function, which attempts to fit the empirical data to a parametric probability distribution.

- The fitted distribution can then be used to analytically approximate the cumulative distribution function $F_{P_r^T}(\tau)$, and thus estimate the probability $\mathbb{P}(P_r^T > \tau)$ with improved accuracy.

- Among the candidate distributions tested, the Gamma distribution provided the best fit to the empirical data of the total received power P_r^T.

- The probability density function (PDF) of the Gamma distribution is given by:

$$f(x) = \frac{1}{\Gamma(k)\theta^k} x^{k-1} e^{-x/\theta}, \quad x > 0 \tag{6.8}$$

  where:

  - $k > 0$ is the shape parameter,
  - $\theta > 0$ is the scale parameter,
  - $\Gamma(k)$ is the Gamma function defined as:

$$\Gamma(k) = \int_0^\infty t^{k-1} e^{-t} dt. \tag{6.9}$$

- The cumulative distribution function (CDF) is:

$$F_{P_r^T}(x) = \frac{1}{\Gamma(k)} \gamma\left(k, \frac{x}{\theta}\right) \tag{6.10}$$

  where $\gamma(k, x)$ is the lower incomplete Gamma function:

$$\gamma(k, x) = \int_0^x t^{k-1} e^{-t} dt \tag{6.11}$$

- To analytically determine the Gamma parameters, we must compute the mean $\mu = \mathbb{E}[P_r^T]$ and variance $\sigma^2 = \mathrm{Var}(P_r^T)$ of the total received power.

- We have:
$$P_r^T = \sum_{\phi_i} P_{r_i} = \sum_{\phi_i} \frac{P}{1 + K d_i^6} \tag{6.12}$$

- Using Campbell's theorem for a homogeneous Poisson point process of density λ, the expectation becomes:
$$\mathbb{E}[P_r^T] = \lambda \int_{\mathbb{R}^2} \frac{P}{1 + K d(x)^6} \, dx \tag{6.13}$$

- Assuming circular symmetry and that the transmitter-receiver 3D distance is as show in Equation 6.4, the expression simplifies to:
$$\mathbb{E}[P_r^T] = 2\pi\lambda \int_0^{R_{\text{sim}}/\sqrt{2}} \frac{P \cdot R}{1 + K(R^2 + H^2)^3} \, dR \tag{6.14}$$

- Similarly, the variance is given by:
$$\text{Var}(P_r^T) = 2\pi\lambda \int_0^{R_{\text{sim}}/\sqrt{2}} \left(\frac{P}{1 + K(R^2 + H^2)^3} \right)^2 R \, dR \tag{6.15}$$

- Once the mean μ and variance σ^2 are computed, the Gamma distribution parameters are:
$$k = \frac{\mu^2}{\sigma^2} \quad \text{(shape)} \tag{6.16}$$
$$\theta = \frac{\sigma^2}{\mu} \quad \text{(scale)} \tag{6.17}$$

- Since the integrals involved in the computation of the mean and variance (6.14 and 6.15) are too complex to solve analytically, we evaluated them numerically using MATLAB. The results are:
  - $\mathbb{E}[P_r^T] = \mu = 0.5243$
  - $\text{Var}[P_r^T] = \sigma^2 = 0.0423$

- Given the relationships in 6.16 and 6.17, we obtain the following parameters for the Gamma distribution:
  - $k = 6.4969$
  - $\theta = 0.0807$

- These values provide a fully specified Gamma model for the total received power, which can now be used to estimate the wake-up success probability analytically via 6.7

- Thus, the analytical expression of the successful wake-up probability is given by:
$$\mathbb{P}(P_r^T > \tau) = 1 - \frac{1}{\Gamma(k)} \gamma\left(k, \frac{\tau}{\theta}\right) \tag{6.18}$$

  where:

- $k = 6.4969$
- $\theta = 0.0807$

- Figure6.9 demonstrates the fit between the empirical distribution of the total received power and the Gamma distribution. The analytical fit closely follows the empirical histogram, justifying the use of the Gamma model.

- Figure6.10 compares the analytical expression of the wake-up probability with the results from Monte Carlo simulations (Figure 6.2). The strong agreement between the two curves further confirms the validity of the analytical formulation derived earlier.

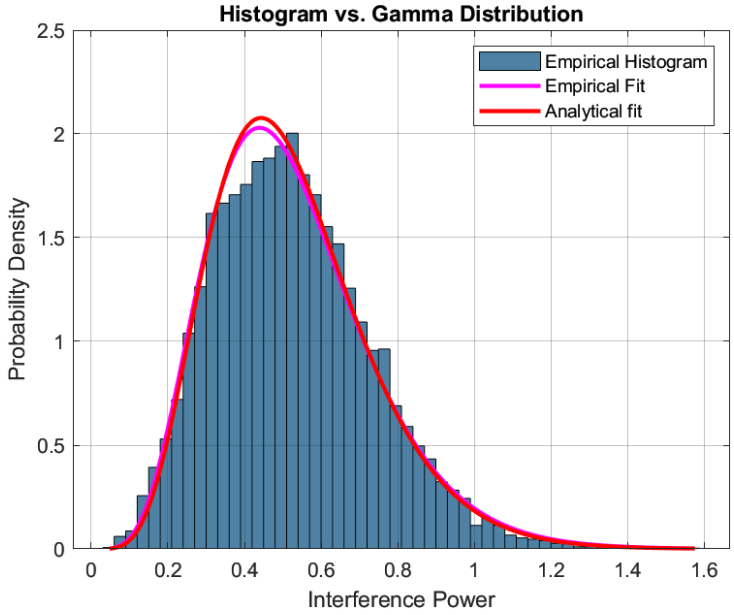

Figure 6.9: Empirical histogram of the total received power P_r^T based on Monte Carlo simulations, along with the fitted Gamma distribution.

6.5.2 Probability of False Wake-Up

- For the false wake-up probability, we follow the same approach as for the successful wake-up. However, instead of computing the total received power from all the above-ground nodes, we only consider the interference, which is the sum of received powers from all *non-serving* nodes.

$$\mathbb{E}[I] = \mathbb{E}\left[\sum_{\phi_i \setminus r_0} \frac{P}{1 + K \times d_i^6}\right] = \lambda \int_{r_0}^{R_{\text{sim}}/\sqrt{2}} \frac{P \cdot R}{1 + K \times (R^2 + H^2)^3}\, dR \tag{6.19}$$

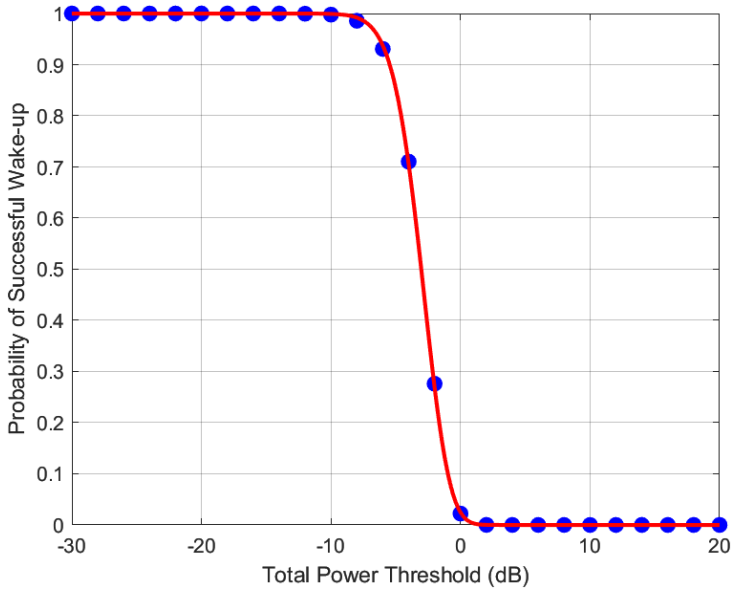

Figure 6.10: Comparison of Analytical and Monte Carlo Results for the Probability of Successful Wake-up

$$\mathrm{Var}[I] = \lambda \int_{r_0}^{R_{\mathrm{sim}}/\sqrt{2}} \left(\frac{P}{1 + K \times (R^2 + H^2)^3} \right)^2 RdR \tag{6.20}$$

- However, since the distance to the nearest above-ground node, denoted r_0, is a random variable, we must take the expectation over its distribution to compute the mean interference:
- Consider a PPP in $\mathbb{R}^2$ with intensity λ having units of points/area. If $\mathbf{A}$ is a set denoting a circle of radius r, we would have $l(A) = \pi r^2$ and $\mu(\mathbf{A}) = \lambda \pi r^2$.
- The probability that there are exactly n nodes in area $\mathbf{A}$ is given by the Poisson distribution: [21]

$$\mathbb{P}[\Phi(\mathbf{A}) = n] = \frac{(\lambda \pi r^2)^n}{n!} e^{-\lambda \pi r^2} \tag{6.21}$$

- Now, define r_0 as the random distance between a typical underground node and its nearest (serving) above-ground node. Since the underground node always connects to its closest above-ground node, no other nodes can be located within the disk of radius r_0.
- Thus, the probability that there is no above-ground node within a radius r_0 is: [21]

$$\mathbb{P}[r > r_0] = \mathbb{P}[\text{No BS closer than } r] = e^{-\lambda \pi r_0^2} \tag{6.22}$$

- This is the complementary cumulative distribution function (CCDF) of r_0. The corresponding cumulative distribution function (CDF) is: [21]

$$F_{r_0}(r) = \mathbb{P}[r \leq r_0] = 1 - e^{-\lambda \pi r_0^2} \tag{6.23}$$

- Differentiating the CDF gives the probability density function (PDF): [21]

$$f_{r_0}(r) = \frac{dF_{r_0}(r)}{dr} = 2\pi\lambda r_0 e^{-\lambda\pi r_0^2} \tag{6.24}$$

- Conditioning on the nearest above-ground node being at a distance r from the typical user, the expectation of the interference can be written as:

$$\mathbb{E}[I] = \mathbb{E}_{r_0}[\mathbb{E}[I|r_0 = r]] = \int_{r>0}^{R_{\text{sim}}/\sqrt{2}} \mathbb{E} f_{r_0}(r) dr \tag{6.25}$$

- Using the distribution $f_{r_0}(r)$ derived in 6.24, we get:

$$\mathbb{E}[I] = \int_0^{Rsim/\sqrt{2}} f_{r0}(r)[\lambda \int_r^{Rsim/\sqrt{2}} \frac{P}{1 + K \times (R^2 + H^2)^3} RdR]dr \tag{6.26}$$

- Similarly:

$$\text{Var}[I] = \int_0^{Rsim/\sqrt{2}} f_{r0}(r)[\lambda \int_r^{R_{\text{sim}}/\sqrt{2}} \left(\frac{P}{1 + K \times (R^2 + H^2)^3}\right)^2 RdR]dr \tag{6.27}$$

- Once again, the integrals 6.26 and 6.27 are evaluated numerically using MATLAB. The results are:
  - $\mathbb{E}[I] = \mu = 0.39585$
  - $\text{Var}[I] = \sigma^2 = 0.024554$
- Given the relationships in 6.16 and 6.17, we obtain the following parameters for the Gamma distribution:
  - $k = 6.3818$
  - $\theta = 0.0620$
- Figure 6.11 shows the empirical histogram of the total interference power compared to its Gamma approximation. While the fit is not as precise as in the successful wake-up case, the analytical distribution still closely follows the general shape of the empirical data, making the Gamma model a reasonable and usable approximation.
- Figure 6.12 compares the analytical expression of the false wake-up probability with Monte Carlo simulation results (Figure 6.3). Although the agreement is slightly less tight than in the successful wake-up scenario, the analytical curve remains close enough to validate the model and justify its use for performance evaluation.

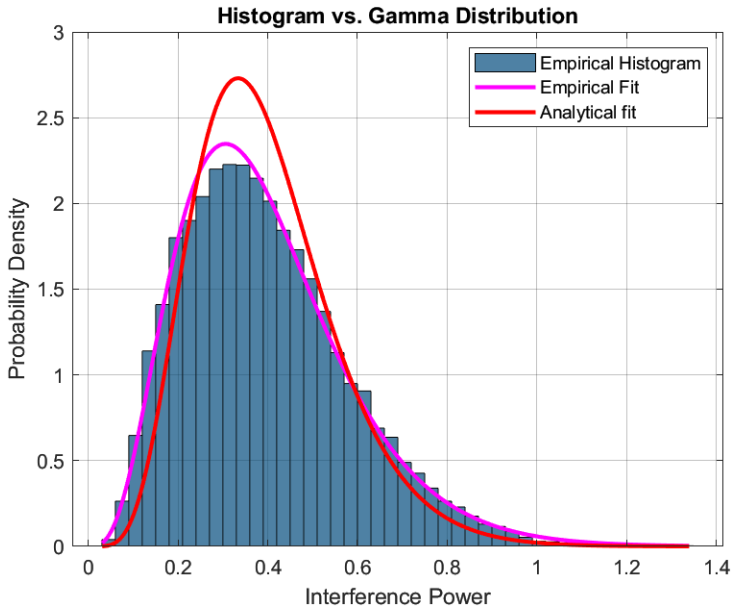

Figure 6.11: Empirical histogram of the total interference P_r^T based on Monte Carlo simulations, along with the fitted Gamma distribution.

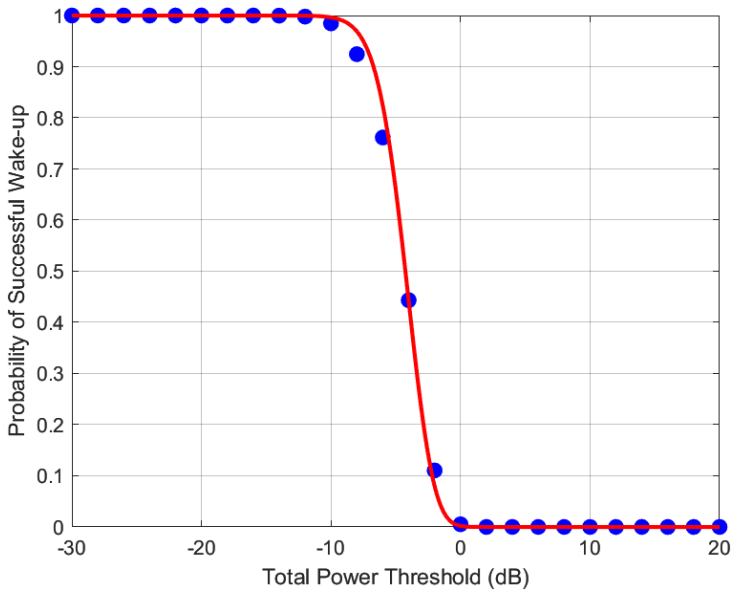

Figure 6.12: Comparison of Analytical and Monte Carlo Results for the Probability of False Wake-up

6.6 Results Discussion

The analysis reveals that the probabilities of successful and false wake-up are closely correlated and are influenced similarly by system parameters. This suggests that improving the likelihood of waking up the intended underground node inherently increases the risk of unintentionally activating neighboring nodes.

This dual sensitivity poses a significant challenge in designing reliable magnetic induction wake-up systems, where selectivity is crucial. To address this issue, the following mitigation strategies can be employed:

- **Receiver Identification:** Assign each receiver a unique ID and embed it in the wake-up signal. A node would only fully wake up if it receives both the wake-up signal and its own ID.
- **Beamforming:** Focus the transmitted power directionally toward the intended receiver to reduce the power received by nearby nodes, thus lowering their false wake-up probability. In a related study [22], a beamforming technique using Mutual Information (MI) was proposed, which optimizes the transmission direction to further enhance the accuracy of wake-up detection while minimizing interference from surrounding nodes.

6.7 Conclusion

This chapter highlighted the value of large-scale analysis in evaluating underground magnetic induction communication networks. Using stochastic geometry, we modeled the random distribution of transmitters and derived probabilities for successful and false wake-ups. These results were validated through Monte Carlo simulations, confirming the accuracy of our approach. This large-scale perspective complements our experiments and offers key insights for designing scalable and reliable systems.

Chapter 7

Conclusion and Future Work

In this work, we presented a novel, power-efficient, and scalable solution for underground communication within the IoUgT framework. The primary challenge addressed was the severe signal attenuation and variability of underground propagation conditions, which hinder the deployment of traditional wireless systems. By leveraging MI communication, we proposed an architecture that is robust to soil composition and moisture variability and avoids the typical multi-path limitations of electromagnetic waves.

Our system decouples underground sensing from long-range communication through the integration of passive surface nodes and mobile UAV data collectors. Ultra-low-power underground sensors equipped with wake-up receivers remain in deep sleep mode until triggered, significantly reducing energy consumption. Upon receiving a wake-up call, the system activates the transmitter only when necessary, which was shown to dramatically improve battery lifetime. Our experiments demonstrated that the transmitter can reach lifetimes exceeding 15 years under low transmission frequency when powered by commercial batteries, thanks to this selective wake-up strategy.

Experimental results showed that the system achieves a wake-up range of up to 6.8 meters and reliable data transmission (zero bit error rate) up to 3.8 meters. Although BER performance degrades at longer distances, our findings suggest that shorter data packets could improve range, as shown by the consistent detection of the wake-up signal.

Additionally, to evaluate the feasibility of the system in large-scale deployments, we developed an analytical model using tools from stochastic geometry. This allowed us to derive expressions for key performance metrics and assess the systems scalability in more complex, realistic environments.

Through the combination of practical implementation, empirical validation, and theoretical modeling, this work lays the groundwork for future developments in IoUgT systems.

Future Work includes several promising directions:

- Conducting real-world field experiments using actual UAVs to validate aerial data harvesting under environmental constraints.
- Developing a cloud-based interface to monitor underground data in real-time and remotely trigger wake-up calls.
- Introducing passive relay nodes to extend communication range and increase deployment flexibility.
- Extending the large-scale modeling to include UAV behavior and aerial coverage using stochastic geometry tools.
- Enhancing wake-up selectivity through node ID-based addressing or beamforming to prevent waking up unnecessary underground devices.
- Sending data in small packet sizes to improve communication range and reliability.
- Designing our own custom transmitter and receiver that combines the properties of the modules RF125 Tx and AS3933.

Chapter 8

Bibliography

Bibliography

1. WIKIPEDIA CONTRIBUTORS. *Soil* [https://en.wikipedia.org/wiki/Soil]. 2021. Accessed: June 3rd, 2025.
2. LI, Li; VURAN, Mehmet C.; AKYILDIZ, Ian F. Characteristics of Underground Channel for Wireless Underground Sensor Networks. *IFIP Mediterranean Ad Hoc Networking Workshop (Med-Hoc-Net)*. 2007.
3. SUN, Zhi; AKYILDIZ, Ian F. Magnetic Induction Communications for Wireless Underground Sensor Networks. *IEEE Transactions on Antennas and Propagation*. 2010, vol. 58, no. 7, pp. 2426–2435.
4. PAL, Amitangshu; GUO, Hongzhi; YANG, Sijung; AKKAS, Mustafa Alper; ZHANG, Xufeng. Taking Wireless Underground: A Comprehensive Summary. *ACM Transactions on Sensor Networks*. 2023, vol. 20, no. 1, Article 19, 44 pages. Available from DOI: 10.1145/3587934.
5. SAEED, Nasir; ALOUINI, Mohamed-Slim; AL-NAFFOURI, Tareq Y. Toward the Internet of Underground Things: A Systematic Survey. *IEEE Communications Surveys & Tutorials*. 2019, vol. 21, no. 4, pp. 3443–3466. Available from DOI: 10.1109/COMST.2019.2934365.
6. JAISWAL, Shweta. Dielectric Properties of Soil: A Study of Particle Size Distribution and Mineral Composition. *UFANS International Journal of Food and Nutritional Sciences*. 2021, vol. 10, no. 8. ISSN 2319-1775 (Print), ISSN 2320-7876 (Online). UGC CARE Listed (Group -J) Journal.
7. MUZZAMMIL, Muhammad; KOUZAYHA, Nour; SAEED, Nasir; AL-NAFFOURI, Tareq Y. Towards Sustainable Internet of Underwater Things: UAV-aided Energy Efficient Wake-up Solutions. *IEEE Systems, Man, and Cybernetics Magazine*. 2022. Available also from: https://www.researchgate.net/publication/362943486_Towards_Sustainable_Internet_of_Underwater_Things_UAV-aided_Energy_Efficient_Wake-up_Solutions. Accessed June, 04th 2025.
8. SHAH, G. A. A Survey on Medium Access Control in Underwater Acoustic Sensor Networks. In: *Proceedings of the International Conference on Advanced Information Networking and Applications Workshops (WAINA)*. IEEE, 2009, pp. 1178–1183.
9. STOJANOVIC, M. Underwater Acoustic Communications. In: *Proceedings of IEEE Electro/International 1995*. IEEE, 1995, pp. 435–440.
10. STOJANOVIC, Milica; PREISIG, James C. Underwater Acoustic Communication Channels: Propagation Models and Statistical Characterization. *IEEE Communications Magazine*. 2009, vol. 47, no. 1, pp. 84–89.
11. AL., Yang et. Development of an underground through-soil wireless acoustic communication system. *IEEE Wireless Communications*. 2020.

12. AL., Adnan et. Wireless Underground Sensor Communication Using Acoustic Technology. *Sensors*. 2024.

13. BOGIE, I. S. Conduction and magnetic signalling in the sea: a background review. *Radio and Electronic Engineer*. 1972, vol. 42, no. 10, pp. 555–565.

14. PAL, Amitangshu; KANT, Krishna. NFMI: Connectivity for short-range IoT applications. *Computer*. 2019, vol. 52, no. 2, pp. 63–67.

15. PAL, Amitangshu; KANT, Krishna. NFMI: Near field magnetic induction based communication. *Computer Networks*. 2020, vol. 181, p. 107548.

16. SUN, Zhi; AKYILDIZ, Ian F. Underground Wireless Communication using Magnetic Induction. *IEEE Transactions on Antennas and Propagation*. 2010, vol. 58, no. 7, pp. 2426–2435.

17. TELFORD, W. M.; GELDART, L. P.; SHERIFF, R. E. *Applied Geophysics*. 2nd. Cambridge: Cambridge University Press, 1990.

18. SCOTT, James H. *Electrical and Magnetic Properties of Rock and Soil*. 1983. Open-File Report, 83-915. United States Geological Survey. Prepared in cooperation with the U.S. Air Force.

19. ROHDE SCHWARZ. *Understanding UART* [https://www.rohde-schwarz.com/cz/products/test-and-measurement/essentials-test-equipment/digital-oscilloscopes/understanding-uart_254524.html]. 2025. Accessed June 18, 2025.

20. DFROBOT. *FireBeetle 2 Board ESP32C6* [https://wiki.dfrobot.com/SKU_DFR1075_FireBeetle_2_Board_ESP32_C6]. 2025. Accessed June 18, 2025.

21. ANDREWS, Jeffrey G.; GUPTA, Abhishek K.; DHILLON, Harpreet S. A Primer on Cellular Network Analysis Using Stochastic Geometry. *arXiv preprint arXiv:1604.03183*. 2016. Available also from: https://arxiv.org/abs/1604.03183. Accessed: 2025-06-06.

22. JADIDIAN, Jouya; KATABI, Dina. Magnetic MIMO: How To Charge Your Phone in Your Pocket. *Massachusetts Institute of Technology*. 2014. Available also from: https://courses.grainger.illinois.edu/ece598hh/sp2018/papers/magmimo.pdf. Accessed: 2023-04-15.

Chapter 9

Appendicies

Appendix A

RF125 user instructions

RF125 instructions

RF125-RX

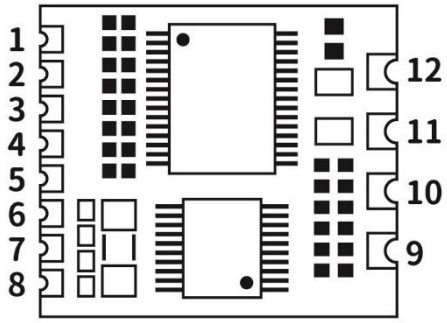

Pin number	Pin definition	I/O	Description
1	PAIR	I	pairing button, pull low for more than 1 second to enter pairing mode, pull high for normal mode
2	TXD	O	Uart Data output
3	RXD	I	Reserved for factory use
4,8,10	GND		Power ground
5	VCC		Can be externally connected with a positive voltage of 2.5-3.6V
6	WAKE UP	O	output high pulse to wake up external device after received effective 125K signal,
7	LED	O	Connected with external LED to indicate the status
9	ANT3	I	External 125K patch antenna, the inductance is 7.2mH
11	ANT2	I	External 125K patch antenna, the inductance is 7.2mH
12	ANT1	I	External 125K patch antenna, the inductance is 7.2mH

RF125-RA

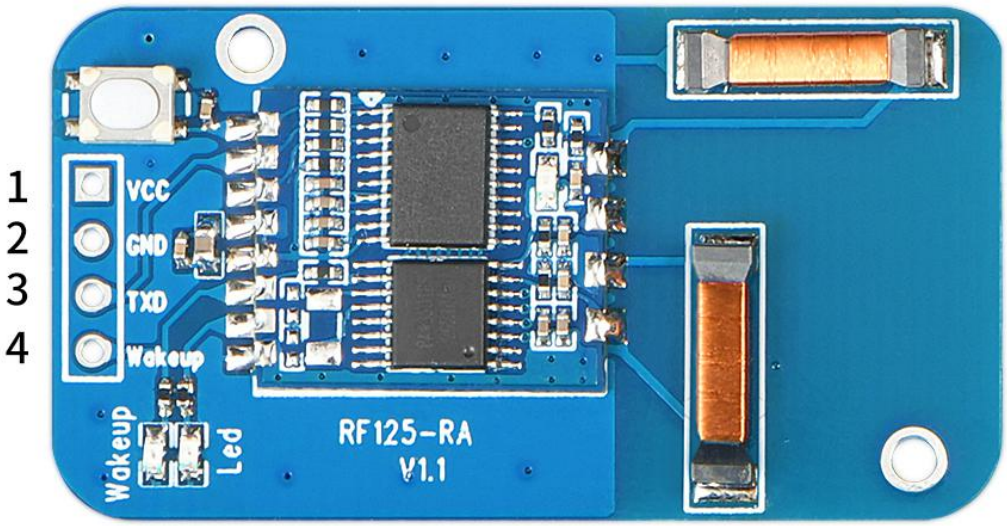

Pin number	Pin definition	I/O	Description
1	VCC		Can be externally connected with a positive voltage of 2.5-3.6V
2	GND		Power ground
3	TXD	O	Data output port
4	WAKE UP	O	After receiving 125K signal, output high pulse

Wiring problem

1. TXD is the output pin of the data packet, which is connected to the RXD of the external device. The UART format is 9600,8,N,1.

2. WAKE UP is the external wake-up pin of RF125-RX. When a data packet is received, a high pulse lasting 50ms is generated, which is used to wake up the external device.

3. RF125-RX has ANT1, ANT2, ANT3 3 antenna pads, customers can connect the antenna according to their own needs. (For RF125-RA, there is antennas on board, no need to connect with antennas more).

Instructions

Power on and wait for data to be received.

RF125-TX

Pin definition	I/O	Voltage	Description
VCC		12-30v	Can be connected to the positive pole of 12-30V power supply
GND		0	Connect the negative pole of the power supply
TXD	O	0-3.3v	Serial output port
RXD	I	0-3.3v	Serial input port

Wiring problem

1. TXD is connected to the RXD of the external device. RXD is connected to the TXD of the external device, and the UART format is 9600, 8, N, 1.

Instructions

After power-on, Set the corresponding parameters before transmission.All the command is ended with 0x0d 0x0a.

Configuration instructions

(1) Set the payload to be transmitted

CMD (1Byte)	Length(1Byte)	Payload(Length Byte)	End code
0x57			0x0d 0x0a

CMD: 1 byte, 0x57

Length: 1 byte, the length of the data packet, not including the command word, this byte and end code. The range is 0~0x2D (a packet can transmit up to 45 (0x2D) bytes)

Payload: data content

Example:

0x57 0x05 0x01 0x02 0x03 0x04 0x05 0x0D 0x0A

Return ： 0x4F 0x4B 0x0D 0x0A

CMD ： 0x57

Length ： 0x05

Payload ： 0x01 0x02 0x03 0x04 0x05

(2) Modify the ID of the transmitter:

Noted: ID greater than 0x7F is regarded as an error

CMD (1Byte)	ID(7Bit)	End code
0x58		0x0d 0x0a

CMD: 1 byte, 0x58

ID: 7 Bits, the range is 0~0x7F, greater than 0x7F is regarded as an error

example:

Set the ID of the transmitter to 0x01

0x58 0x01 0x0D 0x0A

Return: 0x4F 0x4B 0x0D 0x0A

(3) Read out the ID of the transmitter

CMD（1Byte）	End code
0x52	0x0d 0x0a

Example: The ID of the transmitter is 0x01
0x52 0x0D 0x0A
Return:0x01 0x0D 0x0A

(4)Set the time interval (ms) between adjacent transmission. The time interval should be (250ms – 60 000 ms), it will be set as 250ms automatically if it is less than 250ms.

CMD(1Byte)	TIME_H(1Byte)	TIME_L(1Byte)	End code
0x53			0x0d 0x0a

CMD：0x53

TIME_H: The upper 8 bits of the time

TIME_L: the lower 8 bits of the time

Range: 0x00FA~0xEA60, that is, 250ms ~60 seconds.

example:

Set the interval of 1000ms, and the conversion of 1000 into hexadecimal is 0x03e8

The command is: 0x53 0x03 0xe8 0x0D 0x0A

Return: 0x4F 0x4B 0x0D 0x0A

(5)Set the transmitting state of the transmitter

1>**start** transmission

CMD(5Byte)	End code
0x73 0x74 0x61 0x72 0x74	0x0d 0x0a

The command is: 0x73 0x74 0x61 0x72 0x74 0x0D 0x0A

Return: 0x4F 0x4B 0x0D 0x0A

After the command is successfully transmitted, RF125-TX will automatically and continuously transmit data packets according to the set time interval (0x53 command).

2>**stop transmission**

CMD(4Byte)	End code
0x73 0x74 0x6F 0x70	0x0d 0x0a

The command is: 0x73 0x74 0x6F 0x70 0x0D 0x0A

Return: 0x4F 0x4B 0x0D 0x0A

After the command is successfully transmitted, RF125-TX will automatically stop transmitting.

Appendix B

Power profiler kit ii

Power Profiler Kit II

Current measurement tool for embedded development

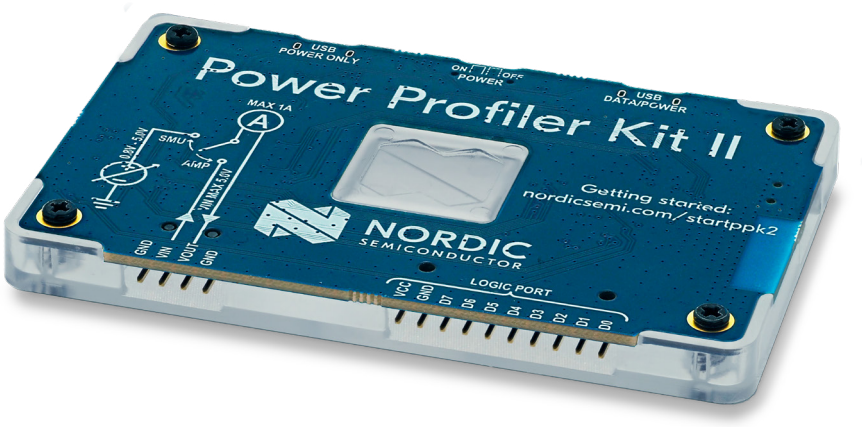

Power Profiling made easy
The Power Profiler Kit II (PPK2) is an easy-to-use tool for current measurements and power consumption optimization of embedded solutions. The PPK2 connectors can be connected to any Nordic DK or custom board as a standalone unit, i.e. there are no requirements for additional kits or debuggers. The PPK2 supports both a source mode and an ampere meter mode.

In the source mode, shown as source measure unit (SMU) on the PCB, the PPK2 both supplies power and measures the current of the external device under test (DUT). The source mode has an on-board regulator capable of supplying up to 1A peak currents. Both modes support VCC levels between 0.8V and 5V. In the ampere meter mode, the DUT is powered by a separate power source.

High accuracy and resolution
The PPK2 has an advanced analog measurement unit with a high dynamic input range. This allows for accurate current consumption measurements for the entire range typically seen in embedded applications, all the way from 200nA to 1A. This allows measuring everything from Power Off mode of the DUT to the maximum power consumption of any Nordic DUT or external HW with headroom to spare for additional circuit draw, e.g. an nRF9160 DK with external sensors.

The resolution varies between 100nA and 1mA, depending on the current measurement range. The time resolution is also high enough to detect spikes. This is achieved by having a 100 ksps sampling rate of the current, 10× the resolution of the long term view of our previous generation PPK.

Improve code debugging
The PPK2 includes support for 8 digital inputs that can be used as a low-end logic analyzer. This makes it possible to instrument the code and make it easy to link the power consumption to blocks of code being executed.

Key features

- 200nA to 1A current measurement range with a resolution that varies between 100nA and 1mA
- Source mode and ampere meter mode
- Source mode includes built-in programmable regulator with a 0.8V to 5V output range and up to 1A current supply
- 100 ksps sampling rate (10 × greater than previous generation)
- Standalone unit
- 8 digital inputs for low-end logic analyzer support
- Measure instantaneous and average current on all Nordic DKs, in addition to custom boards
- Supported through nRF Connect for Desktop's Power Profiler app
- Export measurement data for post-processing

Applications

- Power debugging of embedded applications
- Estimate battery lifetime of completed solution

Kit content

- Power Profiler Kit II board
- 4-pin current measurement cable, 10-pin logic port cable

Needed resources

- nRF Connect for Desktop's Power Profiler app

Order information

nRF-PPK2	Power Profiler Kit II, current measurement tool for embedded development

For more information please visit: **nordicsemi.com/ppk2**

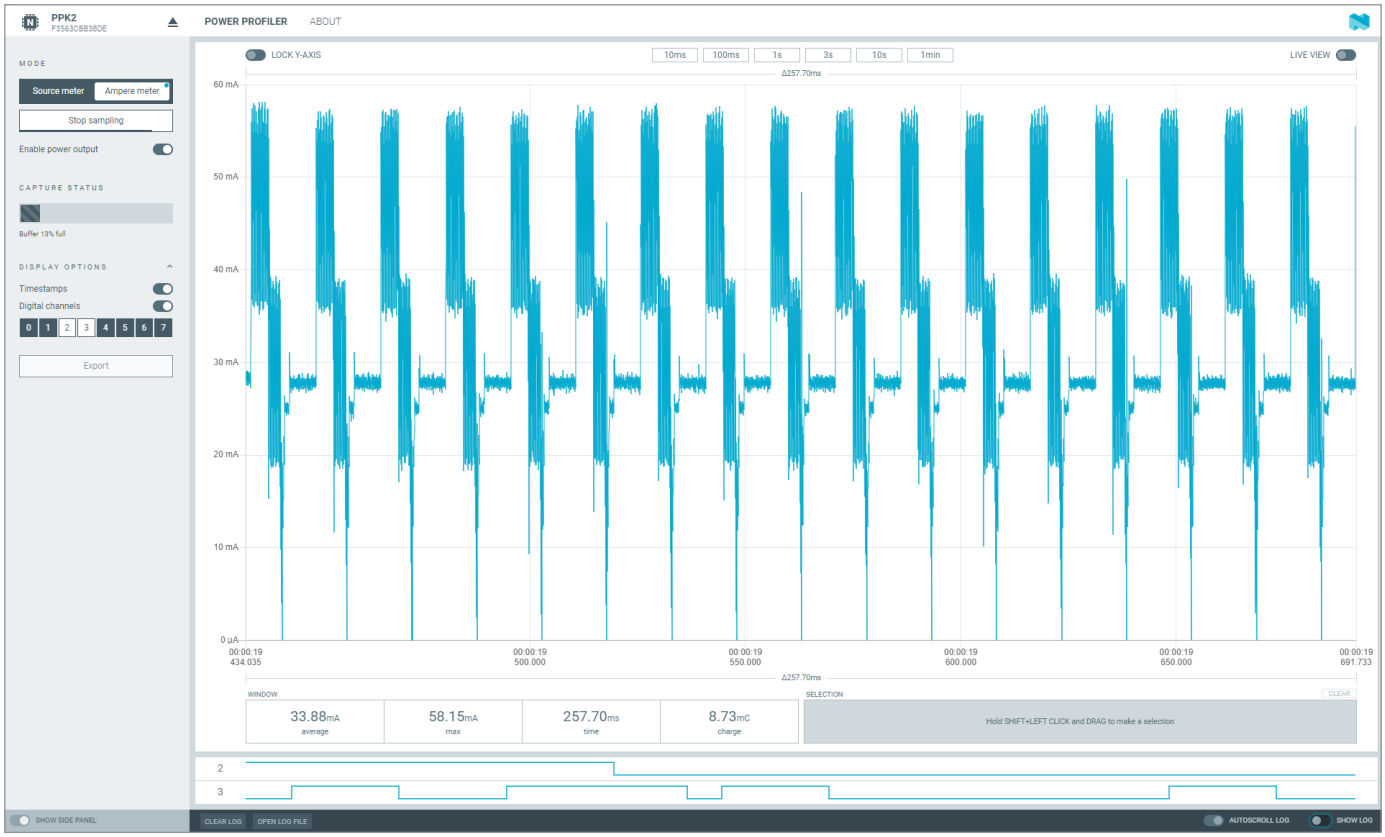

Screenshot of the Power Profiler app running on the nRF9160 DK in ampere meter mode.

Easy to use desktop application
The PPK2 is supported by an nRF Connect for Desktop Power Profiler app for analyzing both average and instantaneous current consumption. It is possible to take readings over an extended duration, while simultaneously zooming in on a millisecond interval of interest. Measured data can also be exported for post-processing.

WORLD WIDE OFFICE LOCATIONS

Headquarters:
Trondheim, Norway
Tel: +47 72 89 89 00

For more information:
Visit nordicsemi.com/products for full overview of our product range.

About Nordic Semiconductor:
Nordic Semiconductor specializes in ultra-low power Bluetooth Low Energy, Thread, Zigbee and proprietary 2.4 GHz, as well as LTE-M and NB-IoT wireless communication technologies for IoT.

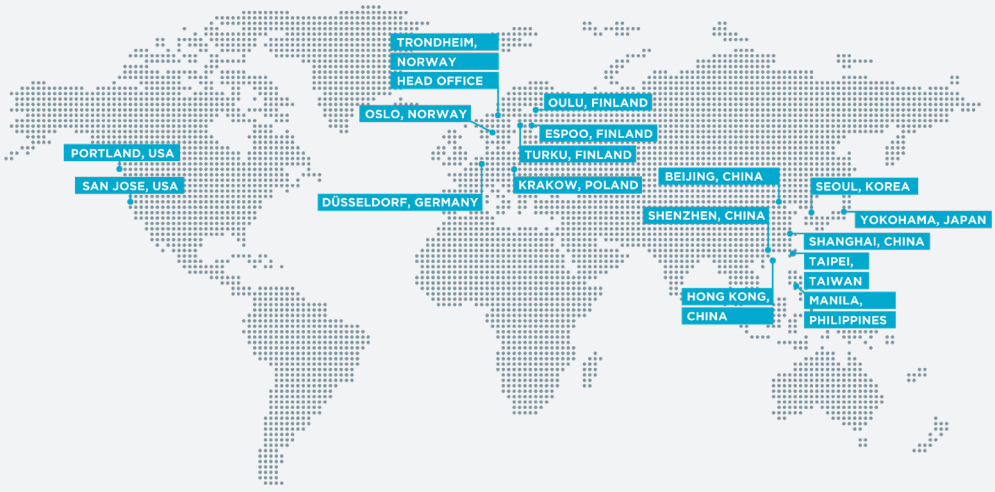

For more information please visit: **nordicsemi.com/ppk2**

Mouser Electronics

Authorized Distributor

Click to View Pricing, Inventory, Delivery & Lifecycle Information:

Nordic Semiconductor:
nRF-PPK2

Appendix C

AS3933 Demo kit user guide and AS3933 Datasheet

For more information about the AS3933, please refer to:
:https://www.sciosense.com/wp-content/uploads/2023/12/AS3933-Demo-kit-User-Guide.pdf.